

LUMINOUS BURIED AGNS AS A FUNCTION OF GALAXY INFRARED LUMINOSITY REVEALED THROUGH SPITZER LOW-RESOLUTION INFRARED SPECTROSCOPY

MASATOSHI IMANISHI¹

National Astronomical Observatory, 2-21-1, Osawa, Mitaka, Tokyo 181-8588, Japan

Astrophysical Journal

ABSTRACT

We present the results of *Spitzer* IRS infrared 5–35 μm low-resolution spectroscopic energy diagnostics of ultraluminous infrared galaxies (ULIRGs) at $z > 0.15$, classified optically as non-Seyferts. Based on the equivalent widths of polycyclic aromatic hydrocarbon emission and the optical depths of silicate dust absorption features, we searched for signatures of intrinsically luminous, but optically elusive, buried AGNs in these optically non-Seyfert ULIRGs. We then combined the results with those of non-Seyfert ULIRGs at $z < 0.15$ and non-Seyfert galaxies with infrared luminosities $L_{\text{IR}} < 10^{12}L_{\odot}$. We found that the energetic importance of buried AGNs clearly increases with galaxy infrared luminosity, becoming suddenly discernible in ULIRGs with $L_{\text{IR}} > 10^{12}L_{\odot}$. For ULIRGs with buried AGN signatures, a significant fraction of infrared luminosities can be accounted for by detected buried AGN and modestly-obscured ($A_{\text{V}} < 20$ mag) starburst activity. The implied masses of spheroidal stellar components in galaxies for which buried AGNs become important roughly correspond to the value separating red massive and blue, less-massive galaxies in the local universe. Our results may support the widely-proposed AGN-feedback scenario as the origin of galaxy downsizing phenomena, where galaxies with currently larger stellar masses previously had higher AGN energetic contributions and star-formation-originating infrared luminosities, and have finished their major star-formation more quickly, due to stronger AGN feedback.

Subject headings: galaxies: active — galaxies: ISM — galaxies: nuclei — galaxies: Seyfert — galaxies: starburst — infrared: galaxies

1. INTRODUCTION

Infrared sky surveys have discovered a large number of galaxies that are bright in the infrared ($L_{\text{IR}} > 10^{11}L_{\odot}$). They are called luminous infrared galaxies (LIRGs), or ultraluminous infrared galaxies (ULIRGs) when the infrared luminosity exceeds $L_{\text{IR}} > 10^{12}L_{\odot}$ (Sanders & Mirabel 1996). The spectral energy distributions of (U)LIRGs are dominated by infrared emission, which means that luminous energy sources are hidden behind dust. The bulk of the energetic radiation from the energy sources is absorbed by the surrounding dust. Then, the heated dust grains emit this energy as infrared dust emission. The energy sources can be nuclear fusion inside rapidly formed stars (starbursts), the release of gravitational energy produced by mass accreting supermassive black holes (SMBHs) (i.e., AGN activity), or some combination. The importance of (U)LIRGs to the cosmic energy output increases rapidly with increasing redshift (Le Floc'h et al. 2005; Perez-Gonzalez et al. 2005; Caputi et al. 2007). Thus, understanding the hidden energy sources of (U)LIRGs is closely related to clarifying the history of star formation and SMBH growth in the dust-obscured portion of the universe. Since obtaining high quality data of distant ($z > 0.5$) (U)LIRGs is not simple with existing observational facilities, detailed studies of nearby ($z < 0.3$) (U)LIRGs continue to play an important role in understanding the properties of the (U)LIRG population in the universe.

Observations of nearby (U)LIRGs suggest that the

properties of dust-obscured energy sources differ between LIRGs with $L_{\text{IR}} = 10^{11-12}L_{\odot}$ and ULIRGs with $L_{\text{IR}} > 10^{12}L_{\odot}$. First, the fraction of optical Seyferts² systematically increases with increasing infrared galaxy luminosity, and is significantly higher in ULIRGs than LIRGs (Veilleux et al. 1999; Goto 2005). Next, in LIRGs, a large fraction of infrared emission comes from spatially extended regions, whereas the infrared dust emission from ULIRGs is dominated by a spatially compact component (Soifer et al. 2000, 2001). This suggests that much of the dust in LIRGs is heated by stars distributed over spatially extended galactic regions, while in ULIRGs, a large amount of dust is concentrated in the nuclear regions and heated by spatially compact energy sources. Since a mass-accreting SMBH can produce high luminosity from a compact area (< 1 pc), an AGN is a plausible source for compact dust emission in ULIRG nuclei, although very compact starbursts are still a possibility.

The higher fraction of optical Seyferts and higher nuclear dust concentration in ULIRGs than LIRGs are difficult to explain using the scenario that the energetic role of starbursts and AGNs are similar for LIRGs and ULIRGs. In optical Seyferts, lines of sight along the torus axis are relatively transparent to AGN ionizing radiation, and narrow line regions, photoionized by the central AGN radiation, should develop at the 10–1000 pc scale, above a torus scale height. Since narrow-line regions produce optical emission lines whose flux ratios differ from those in clouds photoionized by stars, the pres-

Electronic address: masa.imanishi@nao.ac.jp

¹ Department of Astronomy, School of Science, Graduate University for Advanced Studies, Mitaka, Tokyo 181-8588

² We denote optical Seyferts as luminous AGNs whose accretion disk and broad line regions are thought to be surrounded by torus-shaped dusty obscuring medium, responsible for absorbing the nuclear radiation along some lines of sight.

ence of such luminous AGNs surrounded by torus-shaped dust is easily recognizable through optical spectroscopy (Veilleux & Osterbrock 1987; Kewley et al. 2006). As a larger amount of dust concentrates in the nuclear regions of ULIRGs, even the direction of the lowest dust column density can be opaque to AGN ionizing radiation, blocking the radiation at the inner part (<10 pc) in almost all directions. Such *buried* AGNs lack well-developed narrow-line regions and so are classified optically as non-Seyferts (Imanishi et al. 2007, 2008). Thus, with increasing dust concentration around ULIRG nuclei, it is expected that the fraction of buried AGNs (= optical non-Seyferts) increases, while that of optical Seyferts decreases. This is contrary to observations. The increasing fraction of detectable optical Seyferts in ULIRGs can be explained if the energetic importance of AGNs intrinsically increases in ULIRGs. Specifically, even if the narrow-line regions under-develop, if the intrinsic AGN luminosities increase, then AGN-signature optical detection relative to stellar emission becomes easier, increasing the fraction of optical Seyferts. If this is the case, a large fraction of ULIRGs should contain luminous, but optically elusive, buried AGNs, and the buried AGN fraction should increase substantially in ULIRGs, compared to LIRGs. Since such luminous buried AGNs can have strong feedback to the surrounding dust and gas, it is very important to understand buried AGNs in ULIRGs, not only to unveil the true nature of the ULIRG population, but also to observationally constrain the AGN-starburst connections in galaxies.

Low-resolution infrared spectroscopy is an effective tool for studying buried AGNs that lack well-developed narrow-line regions (or narrow-line regions are obscured by foreground dust), for the following reasons. First, emission from polycyclic aromatic hydrocarbons (PAHs), seen in infrared spectra at $\lambda_{\text{rest}} = 3\text{--}25$ μm in the rest-frame, can be used to distinguish between a buried AGN and a normal starburst (Genzel et al. 1998; Imanishi & Dudley 2000). In a normal starburst with moderate metallicity (>0.3 solar), consisting of UV-emitting HII regions, molecular gas and dust, and photo-dissociation regions (PDRs), PAHs are excited by far-UV photons from stars, and strong PAH emission is produced in PDRs (Sellgren 1981; Wu et al. 2006). When stellar energy sources and dust are spatially well mixed, the flux of both PAH emission and the nearby continuum are similarly attenuated, so that the equivalent width of the PAH emission is insensitive to dust extinction. Thus, a normal starburst with PDRs should always show large equivalent width PAH emission, regardless of the amount of dust extinction. In a pure buried AGN, PAHs are destroyed by strong X-ray radiation from the AGN (Voit 1992; Siebenmorgen et al. 2004); thus, no PAH emission is seen. Instead, a PAH-free continuum from hot, submicron-sized dust grains heated by the AGN is observed. In a starburst/AGN composite galaxy, PAH emission is seen if starbursts occur at locations that are sufficiently shielded from the AGN X-ray radiation. However, the PAH-equivalent width will be smaller than in a pure starburst because of the dilution by PAH-free continuum produced by the AGN. Thus, we can, in principle, disentangle a buried AGN from a normal starburst based on infrared spectral shapes.

Second, a buried AGN and a normal starburst are

distinguishable based on the optical depths of dust absorption features at different wavelengths. In a normal starburst, the energy sources (stars) and gas/dust are spatially well mixed (Puxley 1991; McLeod et al. 1993; Forster Schreiber et al. 2001), whereas in a buried AGN the energy source (= the central accreting SMBH) is very compact and more centrally concentrated than the surrounding gas and dust (Soifer et al. 2000; Imanishi & Maloney 2003; Siebenmorgen et al. 2004) (see also Figures 1a and 1b of Imanishi et al. 2007). The difference in geometry is reflected in two features in the observed low-resolution infrared spectra. First, while the absolute optical depths of dust absorption features in the 3–10 μm range cannot exceed a certain threshold in a normal starburst with mixed dust/source geometry, they can be arbitrarily large in a buried AGN (Imanishi & Maloney 2003; Imanishi et al. 2006, 2007; Levenson et al. 2007). Second, a buried AGN shows a strong dust temperature gradient, in which inner dust, closer to the central energy source, has a higher temperature than outer dust; a normal starburst does not. The presence of this dust temperature gradient can be investigated observationally by comparing the optical depths of dust absorption features at different infrared wavelengths (Dudley & Wynn-Williams 1997; Imanishi 2000; Imanishi et al. 2006, 2007).

Since the PAH emission and dust absorption features are spectrally very broad, low-resolution ($R = 50\text{--}100$) infrared spectroscopy is adequate. We can thus examine fainter sources than high-resolution ($R > 500$) infrared spectroscopy (Farrah et al. 2007), in terms of sensitivity. Imanishi et al. (2007) performed infrared 5–35 μm low-resolution spectroscopic investigations of ULIRGs at $z < 0.15$, classified optically as non-Seyferts, using *Spitzer* IRS, and found buried AGN signatures in a significant fraction of the observed ULIRGs. However, the infrared luminosities of most of the observed ULIRGs are in a narrow range of $L_{\text{IR}} = 10^{12\text{--}12.3}L_{\odot}$, hampering analysis of buried AGNs as a function of galaxy infrared luminosity. It is known that the fraction of optical Seyferts increases with ULIRGs with $L_{\text{IR}} \geq 10^{12.3}L_{\odot}$, compared to those with $L_{\text{IR}} = 10^{12\text{--}12.3}L_{\odot}$ (Veilleux et al. 1999). A similar analysis of buried AGNs in ULIRGs with $L_{\text{IR}} \geq 10^{12.3}L_{\odot}$ will help elucidate the nature of the ULIRG population.

In this paper, we present a systematic, uniform analysis of *Spitzer* IRS infrared 5–35 μm low-resolution spectra of ULIRGs at $z > 0.15$, optically classified as non-Seyferts. By extending our study to ULIRGs at $z > 0.15$, many ULIRGs with $L_{\text{IR}} \geq 10^{12.3}L_{\odot}$ will be included, enabling meaningful comparison of the buried AGN fraction between ULIRGs with $L_{\text{IR}} = 10^{12\text{--}12.3}L_{\odot}$ and $L_{\text{IR}} \geq 10^{12.3}L_{\odot}$. Throughout this paper, $H_0 = 75$ $\text{km s}^{-1} \text{Mpc}^{-1}$, $\Omega_{\text{M}} = 0.3$, and $\Omega_{\Lambda} = 0.7$ are adopted, to be consistent with our previously published papers.

2. TARGETS

We selected our targets from the *IRAS* 1 Jy sample (Kim & Sanders 1998). This 1 Jy sample lists 48 ULIRGs at $z > 0.15$. Based on the optical spectral classifications by Veilleux et al. (1999 Table 2), 33 ULIRGs are classified optically as non-Seyferts (i.e., LINERs, HII regions, and unclassified), and the remaining 15 ULIRGs are classified optically as Seyferts. Since our primary scientific goal is to study buried AGNs, these 33 opti-

cal non-Seyfert ULIRGs are our main targets. Of the 33 ULIRGs, 15 and 12 ULIRGs are classified optically as LINERs and HII-regions, respectively, and 6 ULIRGs are optically unclassified. We analyzed the spectra of 10 LINER, 6 HII-region, and 4 unclassified ULIRGs. These 20 ($= 10 + 6 + 4$) ULIRGs cover $>60\%$ of 33 optically non-Seyfert ULIRGs at $z > 0.15$, and should be unbiased in terms of their dominant energy sources. Table 1 summarizes the basic information and *IRAS*-based infrared properties of the observed optically non-Seyfert ULIRGs. Although only 8 out of 48 non-Seyfert ULIRGs at $z < 0.15$ studied by Imanishi et al. (2007) have $L_{\text{IR}} \geq 10^{12.3} L_{\odot}$, 17 out of 20 observed non-Seyfert ULIRGs at $z > 0.15$ show $L_{\text{IR}} \geq 10^{12.3} L_{\odot}$ (Table 1), substantially increasing the number of ULIRGs with $L_{\text{IR}} \geq 10^{12.3} L_{\odot}$.

3. OBSERVATIONS AND DATA ANALYSIS

Observations of all 20 ULIRGs were performed using the Infrared Spectrograph (IRS) (Houck et al. 2004) onboard the Spitzer Space Telescope (Werner et al. 2004). All four modules, Short-Low 2 (SL2; 5.2–7.7 μm) and 1 (SL1; 7.4–14.5 μm), and Long-Low 2 (LL2; 14.0–21.3 μm) and 1 (LL1; 19.5–38.0 μm) were used to obtain full 5–35 μm low-resolution ($R \sim 100$) spectra. Table 2 details the observing log. The slit width was $3''.6$ or 2 pixels for SL2 ($1''.8 \text{ pixel}^{-1}$) and $3''.7$ or ~ 2 pixels for SL1 ($1''.8 \text{ pixel}^{-1}$). For LL2 and LL1, the slit widths were $10''.5$ and $10''.7$, respectively, corresponding to ~ 2 pixels for both LL2 ($5''.1 \text{ pixel}^{-1}$) and LL1 ($5''.1 \text{ pixel}^{-1}$).

The latest pipeline-processed data products at the time of our data analysis were used. Frames taken at position A were subtracted from those taken at position B to remove background emission, mostly the zodiacal light. Spectra were then extracted in a standard manner. Apertures with 4–5 pixels were employed for SL and LL data, depending on the spatial extent of individual sources. Then, spectra extracted for the A and B positions were summed. Wavelength calibration was made based on the files of the *Spitzer* pipeline processed data, named “b0_wavsamp.tbl” and “b2_wavsamp.tbl” for SL and LL, respectively. These data are believed to be accurate within 0.1 μm . A small level of error in wavelength calibration will not affect our main conclusions. Since emission from all ULIRGs is dominated by spatially compact sources at the observed wavelength, flux calibration was performed using the *Spitzer* pipeline processed files “b0_fluxcon.tbl” (SL) and “b2_fluxcon.tbl” (LL). For SL1 spectra, data at $\lambda_{\text{obs}} > 14.5 \mu\text{m}$ in the observed frame are invalid (Infrared Spectrograph Data Handbook Version 1.0) and were discarded. For LL1 spectra, we used only data at $\lambda_{\text{obs}} < 35 \mu\text{m}$ because the data point scatter was large at $\lambda_{\text{obs}} > 35 \mu\text{m}$ and we did not need data at $\lambda_{\text{obs}} > 35 \mu\text{m}$ for our scientific discussions. No defringing was attempted.

For flux calibration, we adopted the values of the pipeline processed data. We made no attempt to recalibrate our spectra using *IRAS* measurements at 12 μm and 25 μm , because only upper limits are provided for *IRAS* 12 μm and/or 25 μm photometry in many of the observed ULIRGs (Table 1). Hence, the absolute flux calibration is dependent on the accuracy of the pipeline processed data, which is taken to be $<20\%$ for SL and LL (Infrared Spectrograph Data Handbook). This level of flux uncertainty will not significantly affect our main

conclusions. In fact, in all cases, the *Spitzer* IRS 25 μm flux agrees within 20% to, or is smaller than, the *IRAS* 25 μm data. For ULIRGs with *IRAS* non-detection at 25 μm , the measured *Spitzer* IRS 25 μm flux is always smaller than the *IRAS* upper limits.

For a fraction of the observed ULIRGs, slight flux discrepancies between SL1 and LL2 were discernible, ranging from 30% to 60%. When the discrepancy was present, the SL1 flux ($3''.7$ wide slit) was always smaller than the LL2 flux ($10''.5$). In these cases, we adjusted the smaller SL1 (and SL2) flux to match the larger LL2 flux. Appropriate spectral binning with 2 or 4 pixels was applied to reduce the scatter of data points at SL2 (5.2–7.7 μm) for some faint ULIRGs, and at $\lambda_{\text{obs}} \sim 10 \mu\text{m}$ for ULIRGs that display very strong 9.7 μm silicate dust absorption features.

4. RESULTS

Figure 1 presents the infrared 5–35 μm low-resolution spectra of the observed 20 ULIRGs. For most of the sources, full 5–35 μm spectra are shown here for the first time.

The spectra in Figure 1 are suitable for displaying the properties of overall 5–35 μm spectral shapes and the 9.7 μm and 18 μm silicate dust absorption features. However, they are not very useful for PAH emission features. Figure 2 presents enlarged spectra at $\lambda_{\text{obs}} = 5.2\text{--}14.5 \mu\text{m}$ to better exhibit the properties of the PAH emission features.

4.1. PAH emission

The majority of ULIRGs in Figure 2 show clearly detectable PAH emission features at $\lambda_{\text{rest}} = 6.2 \mu\text{m}$, 7.7 μm , and 11.3 μm . To estimate the strengths of these PAH emission features, we adopted a linear continuum, following Imanishi et al. (2007) who made systematic and detailed analysis of *Spitzer* IRS infrared 5–35 μm low-resolution spectra of optically non-Seyfert ULIRGs at $z < 0.15$. For the 6.2 μm , 7.7 μm , and 11.3 μm PAH emission features, data at $\lambda_{\text{rest}} = 6.1 \mu\text{m}$ and 6.45 μm , 7.3 and 8.1 μm , and 11.0 μm and 11.6 μm , were used, respectively, to determine linear continuum levels, shown as solid lines in Figure 2. PAH emission features, above the adopted continuum levels, were fitted with Gaussian profiles. The observed rest-frame equivalent widths (EW_{PAH}) and luminosities of the 6.2 μm , 7.7 μm , and 11.3 μm PAH emission features, based on our adopted continuum levels, are summarized in Table 3. The uncertainties coming from the fittings are unlikely to exceed 30%.

As noted by Imanishi et al. (2007), we estimate the strengths of the 7.7 μm PAH emission feature in such a way that the uncertainties caused by the strong, broad 9.7 μm silicate dust absorption feature are minimized. Since our continuum definition is significantly different from those employed in previous papers (e.g., Genzel et al. 1998), readers must be careful when our value is compared with other estimates in the literature. For this reason, although the 7.7 μm PAH emission strength is shown for reference in this paper, it will not play an important part in our discussions, which will be based primarily on the 6.2 μm and 11.3 μm PAH emission strengths.

4.2. Silicate absorption

To estimate the strengths of silicate dust absorption features, we used $\tau'_{9.7}$ and τ'_{18} , defined by Imanishi et al. (2007). The $\tau'_{9.7}$ value is the optical depth of the 9.7 μm silicate absorption feature against a power-law continuum determined from data points at $\lambda_{\text{rest}} = 7.1 \mu\text{m}$ and 14.2 μm . The τ'_{18} value is the optical depth of the 18 μm silicate absorption feature against a power-law continuum determined from data points at $\lambda_{\text{rest}} = 14.2 \mu\text{m}$ and 24 μm . These continua are shown as dotted lines in Figure 1. Since these continuum levels were determined using data points just outside the 9.7 μm and 18 μm features, close to the absorption peaks, the measured optical depths were well-defined as dips relative to the nearby continuum emission. The $\tau'_{9.7}$ values for all ULIRGs are shown in Table 4 (column 2). The τ'_{18} values are also shown in Table 4 (column 3) for ULIRGs where the 18 μm silicate feature is clearly seen in absorption.

4.3. Ice and CO absorption

A significant fraction of ULIRGs display dips at the shorter wavelength side of the 6.2 μm PAH emission feature. We ascribe the dips to the 6.0 μm H₂O ice absorption feature (bending mode). Figure 3 presents enlarged spectra at $\lambda_{\text{obs}} = 5.2\text{--}9 \mu\text{m}$ for ULIRGs that show this absorption feature clearly. The spectrum of IRAS 12018+1941 is also shown as an example of non-detection of this feature. For ULIRGs with clearly detectable 6.0 μm H₂O ice absorption features, observed optical depths ($\tau_{6.0}$) are summarized in Table 5.

The spectrum of IRAS 00397–1312 in Figure 3 displays a clear CO absorption feature ($\lambda_{\text{rest}} = 4.67 \mu\text{m}$). Its optical depth is also shown in Table 5.

5. DISCUSSION

To study buried AGNs in optically non-Seyfert ULIRGs at $z > 0.15$ and to investigate the buried AGN fraction as a function of ULIRG infrared luminosity, we use the same criteria as applied to non-Seyfert ULIRGs at $z < 0.15$ (Imanishi et al. 2007).

5.1. Magnitudes of detected starbursts

The flux attenuation of continuum emission at $\lambda_{\text{rest}} > 5 \mu\text{m}$, aside from the strong 9.7 μm silicate absorption peak, is small (< 1 mag) for dust extinction with $A_V < 20$ mag (Rieke & Lebofsky 1985; Lutz et al. 1996). Thus, observed PAH emission luminosities can roughly trace the intrinsic luminosities of modestly-obscured ($A_V < 20$ mag) PAH-emitting normal starbursts (with PDRs). Table 3 (columns 8 and 9) tabulates the 6.2 μm PAH to infrared luminosity ratio, $L_{6.2\text{PAH}}/L_{\text{IR}}$, and the 11.3 μm PAH to infrared luminosity ratio, $L_{11.3\text{PAH}}/L_{\text{IR}}$. The ratios in normal starburst galaxies with modest dust obscuration ($A_V < 20$ mag) are estimated to be $L_{6.2\text{PAH}}/L_{\text{IR}} \sim 3.4 \times 10^{-3}$ (Peeters et al. 2004) and $L_{11.3\text{PAH}}/L_{\text{IR}} \sim 1.4 \times 10^{-3}$ (Soifer et al. 2002).

The observed $L_{6.2\text{PAH}}/L_{\text{IR}}$ ratios in the observed ULIRGs (Table 3) range from $< 0.2 \times 10^{-3}$ to 1.4×10^{-3} , or $< 6\%$ to 41% of the value of 3.4×10^{-3} for modestly-obscured starburst galaxies. In the majority of the observed ULIRGs, the ratios are $< 1 \times 10^{-3}$, or $< 30\%$ of 3.4×10^{-3} . Taken at face value, the detected modestly-obscured starbursts in these ULIRGs can account for $< 6\%$ to 41% (mostly $< 30\%$) of their infrared luminosities. The same argument can be applied to the observed

$L_{11.3\text{PAH}}/L_{\text{IR}}$ ratios in ULIRGs. The $L_{11.3\text{PAH}}/L_{\text{IR}}$ ratios are $(0.09\text{--}1.2) \times 10^{-3}$, or 6–86% of the value of 1.4×10^{-3} for modestly-obscured starburst galaxies. In the majority of observed ULIRGs, the ratios are $< 0.7 \times 10^{-3}$ ($< 50\%$ of 1.4×10^{-3}). The observed $L_{11.3\text{PAH}}/L_{\text{IR}}$ ratios suggest that detected modestly-obscured starburst activity can account for 5–86% ($< 50\%$ in most cases) of the infrared luminosities of ULIRGs. When we combine the $L_{6.2\text{PAH}}/L_{\text{IR}}$ and $L_{11.3\text{PAH}}/L_{\text{IR}}$ ratios, we can conclude that the detected modestly-obscured starburst activity is energetically significant (say, 10–50%), but not dominant (say, $> 70\text{--}80\%$) in the observed ULIRGs. The remaining energy sources in these ULIRGs must therefore be (1) highly-obscured ($A_V \gg 20$ mag) starbursts, where the fluxes of PAH emission are substantially attenuated by dust extinction, and/or (2) buried AGNs that produce strong infrared radiation, but virtually no PAH emission.

5.2. ULIRG candidates with luminous buried AGNs

5.2.1. Low equivalent widths of PAH emission features

Whether the dominant energy sources of ULIRG nuclei are highly-obscured normal starbursts or buried AGNs can be determined using the equivalent width of the PAH emission. Since the PAH equivalent width (EW_{PAH}) must always be large in a normal starburst (with PDRs) regardless of the amount of dust extinction, a small EW_{PAH} value suggests contribution from a PAH-free continuum-emitting energy source, namely an AGN (§1).

Following Imanishi et al. (2007), we classify ULIRGs with $EW_{6.2\text{PAH}} < 180$ nm, $EW_{7.7\text{PAH}} < 230$ nm, and $EW_{11.3\text{PAH}} < 200$ nm as sources displaying clear signatures of luminous AGNs. Since these equivalent width values are less than one-third of the typical values for starburst galaxies (Brandl et al. 2006), a substantial contribution from AGN PAH-free continuum emission is indicated. Table 6 (columns 2–4) presents detection or non-detection of buried AGN signatures based on the PAH equivalent width threshold. The buried AGN fraction is much larger based on the small $EW_{6.2\text{PAH}}$ value (14/20; 70%) than on the small $EW_{11.3\text{PAH}}$ value (3/20; 15%). This is reasonable, because the 11.3 μm PAH emission feature is inside the strong 9.7 μm silicate dust absorption feature; thus, buried AGN continuum emission at $\lambda_{\text{rest}} \sim 11.3 \mu\text{m}$ is severely attenuated, not strongly diluting the 11.3 μm PAH emission from modestly-obscured starburst regions (Imanishi et al. 2007).

5.2.2. Absolute optical depths of dust absorption features

Based on the EW_{PAH} values, we can easily detect buried AGNs with very weak starbursts. Even if strong starburst activity is present, *weakly obscured* AGNs are detectable because weakly attenuated PAH-free continuum from the AGNs can dilute the PAH emission considerably. However, detecting *deeply buried* AGNs with co-existing strong starbursts is not easy. Even if the intrinsic luminosities of a buried AGN and surrounding less-obscured starbursts are similar, the AGN flux will be more highly attenuated by dust extinction than the starburst emission, making the observed EW_{PAH} values apparently large.

To determine whether a deeply buried AGN is present

in addition to strong starbursts, we use the optical depths of silicate dust absorption features. As described in §1 and in Imanishi et al. (2007) in more detail, these values can be used to distinguish whether the energy sources are spatially well mixed with dust (a normal starburst), or are more centrally concentrated than the dust (a buried AGN).

In a normal starburst with mixed dust/source geometry, observed flux is dominated by foreground, less-obscured, less-attenuated emission (which shows only weak dust absorption features), with a small contribution from highly-obscured, highly-attenuated emission at the background side of the emitting regions (which shows strong dust absorption features). Thus, the observed optical depths of dust absorption features cannot exceed a certain threshold, unless very unusual dust composition patterns are assumed (Imanishi & Maloney 2003; Imanishi et al. 2006, 2007). In a buried AGN with centrally-concentrated energy source geometry, the foreground screen dust model is applicable, and the observed optical depths can be arbitrarily large. Hence, detection of strong dust absorption features, whose optical depths substantially exceed the upper limit achieved by the mixed dust/source geometry, argues for a foreground screen dust geometry, as expected from a buried AGN (Imanishi & Maloney 2003; Imanishi et al. 2006, 2007). Imanishi et al. (2007) obtained a maximum value of $\tau'_{9.7} < 1.7$ for a normal starburst with mixed dust/source geometry. Considering possible uncertainties in the $\tau'_{9.7}$ estimate ($\sim 10\%$), we classify ULIRGs with $\tau'_{9.7} \geq 2$ as candidates for harboring luminous centrally-concentrated buried AGNs.

In a buried AGN, silicate dust at the very inner part of the obscuring material, close to the central energy source, can be heated to high temperature, show silicate emission, and dilute the silicate absorption feature. Although this dilution may have significant effects on the discussion of $\tau'_{9.7}$ and τ'_{18} for weakly-obscured AGNs (Sirocky et al. 2008), it should not be significant in ULIRGs with large $\tau'_{9.7}$ (= energy sources are highly dust obscured), as studied in this paper. Individual ULIRGs that show buried AGN signatures based on large $\tau'_{9.7}$ values (> 2 ; Table 4) are marked with open circles in Table 6 (column 5).

We have two notes on this method. First, this large $\tau_{9.7}$ method is sensitive to deeply buried AGNs but obviously misses weakly obscured AGNs, which are more easily detected with the above low EW_{PAH} method. Hence, this large $\tau_{9.7}$ method plays a complementary role to the low EW_{PAH} method for the purpose of detecting buried AGN signatures. Second, a normal starburst nucleus with mixed dust/source geometry can produce a large $\tau'_{9.7}$ value, *if* it is obscured by a large amount of foreground screen dust in an edge-on host galaxy (Figure 1d of Imanishi et al. 2007). Although Imanishi et al. (2007) argued that it is very unlikely that the majority of ULIRGs with $\tau'_{9.7} > 2$ correspond to this non-AGN case, some particular ULIRGs could so correspond.

5.2.3. Strong dust temperature gradients

A buried AGN with centrally-concentrated energy source geometry should show a strong dust temperature gradient, in which inner dust, close to the central energy source, has a higher temperature than outer

dust, whereas a normal starburst nucleus with mixed dust/source geometry does not (§1). As explained by Imanishi et al. (2007) in detail, the presence of a strong dust temperature gradient can be detected by comparing the optical depths of $9.7 \mu\text{m}$ and $18 \mu\text{m}$ silicate dust absorption features because the optical depths of dust absorption features at shorter wavelengths probe dust column density toward inner hotter dust than those at longer wavelengths (Figure 2 of Imanishi et al. 2007). Following Imanishi et al. (2007), if an observed $\tau'_{18}/\tau'_{9.7}$ ratio is substantially smaller than $\tau'_{18}/\tau'_{9.7} = 0.3$, the most reasonable explanation is the presence of a strong dust temperature gradient. This can provide additional evidence for centrally-concentrated buried AGNs previously suggested by low EW_{PAH} or large $\tau'_{9.7}$ values (≥ 2).

Table 4 (column 4) summarizes the $\tau'_{18}/\tau'_{9.7}$ ratios for ULIRGs showing clear $18 \mu\text{m}$ silicate absorption (mostly $\tau'_{9.7} > 2$). Table 6 (column 6) displays the detection (or non-detection) of buried AGN signatures, based on this small $\tau'_{18}/\tau'_{9.7}$ method.

5.2.4. Combination of energy diagnostic methods

Table 6 (column 7) summarizes the strengths of the detected buried AGN signatures in *Spitzer* IRS 5–35 μm spectra based on three methods: (1) low PAH equivalent width; (2) large $\tau'_{9.7}$ value; and (3) small $\tau'_{18}/\tau'_{9.7}$ ratio. When buried AGN signatures in individual ULIRGs are consistently found using all or most of these methods, the ULIRGs are classified as *very strong* buried AGN candidates, marked with open double circles. When buried AGN signatures are seen only in the first method, or first and second methods, then the ULIRGs are classified as *strong* AGN candidates (open circles). When the signatures are detected only in the second method, the ULIRGs are classified as *possible* buried AGN candidates (open triangles), as a normal starburst nucleus obscured by foreground dust in an edge-on host galaxy (Figure 1d of Imanishi et al. 2007) cannot be ruled out completely in individual cases.

5.2.5. Absorption-corrected intrinsic luminosities of buried AGNs

For ULIRGs that show buried AGN signatures and small PAH equivalent widths, the observed fluxes are mostly ascribed to AGN-heated PAH-free dust continuum emission. For these ULIRGs, we can estimate the absorption-corrected intrinsic dust emission luminosity at $\sim 10 \mu\text{m}$ (νF_ν) heated by the AGN, based on the observed fluxes at $\lambda_{\text{rest}} \sim 10 \mu\text{m}$ and the dust extinction toward the $10 \mu\text{m}$ continuum emitting regions inferred from $\tau'_{9.7}$ (Imanishi et al. 2007). In a buried AGN with a strong dust temperature gradient, assuming a simple spherical dust distribution, dust emission luminosity is conserved at each temperature from hot inside regions to cool outside regions. Namely, the intrinsic luminosity of inner hot dust emission at $10 \mu\text{m}$ (νF_ν) should be comparable to that of outer cool dust emission at $60 \mu\text{m}$, the wavelength which dominates the observed infrared emission of ULIRGs (Sanders et al. 1988a). Hence, from AGN-originating intrinsic $\nu F_\nu(10 \mu\text{m})$ values, we can quantitatively estimate the energetic contribution from buried AGNs to the infrared luminosities of ULIRGs.

Following Imanishi et al. (2007), we assume that $\tau'_{9.7}$ and the extinction at $\lambda_{\text{rest}} = 8$ or $13 \mu\text{m}$ continuum just

outside the 9.7 μm silicate feature (A_{cont}) are related to $\tau'_{9.7}/A_{\text{cont}} \sim 2.3$ (Rieke & Lebofsky 1985). Based on a foreground screen dust absorption model applicable to buried AGNs, we obtain, as seen in Table 7, absorption-corrected intrinsic AGN luminosities for selected ULIRGs with low PAH equivalent widths. The flux attenuation of the 8 or 13 μm continuum outside the 9.7 μm silicate feature ranges from a factor of 1.7 (IRAS 12018+1941; $\tau'_{9.7} \sim 1.3$) to 3.1 (IRAS 04313–1649; $\tau'_{9.7} \sim 2.8$). The absorption-corrected intrinsic AGN luminosities could explain a significant fraction (15–60%) of the luminosities of these ULIRGs (Table 7).

5.3. Buried AGN fraction as a function of galaxy infrared luminosity

Optically non-Seyfert ULIRGs at $z < 0.15$ studied by Imanishi et al. (2007) mostly display $L_{\text{IR}} = 10^{12-12.3}L_{\odot}$. The extension of our *Spitzer* low-resolution infrared spectroscopic energy diagnostic to ULIRGs at $z > 0.15$ gives a large number ULIRGs with $L_{\text{IR}} \geq 10^{12.3}L_{\odot}$. Specifically, only 8 of 48 observed non-Seyfert ULIRGs at $z < 0.15$ have $L_{\text{IR}} \geq 10^{12.3}L_{\odot}$ (Table 1 of Imanishi et al. 2007), while 17 of 20 observed non-Seyfert ULIRGs at $z > 0.15$ have $L_{\text{IR}} \geq 10^{12.3}L_{\odot}$ (Table 1). We can thus investigate the buried AGN fraction, separating ULIRGs into two categories: those with $L_{\text{IR}} = 10^{12-12.3}L_{\odot}$ and those with $L_{\text{IR}} \geq 10^{12.3}L_{\odot}$.

Figure 4 shows the distribution of $\text{EW}_{6.2\text{PAH}}$, $\text{EW}_{11.3\text{PAH}}$, and $\tau'_{9.7}$ as a function of galaxy infrared luminosity. In addition to ULIRGs, optically non-Seyfert galaxies with $L_{\text{IR}} < 10^{12}L_{\odot}$ (Brandl et al. 2006) are plotted. It is evident that in all plots, the fraction of galaxies which meet the requirement of buried AGNs increases with increasing galaxy infrared luminosity.

To investigate the detectable buried AGN fraction as a function of galaxy infrared luminosity in more detail, we use the combined method (§5.2.4). Based on the classification of non-Seyfert ULIRGs at $z > 0.15$ in Table 6, 13 out of 17 ULIRGs with $L_{\text{IR}} \geq 10^{12.3}L_{\odot}$ show strong buried AGN signatures (open double circles and open circles in column 7 of Table 6), in contrast to only 1 out of 3 ULIRGs with $L_{\text{IR}} = 10^{12-12.3}L_{\odot}$. For non-Seyfert ULIRGs at $z < 0.15$, 5 out of 8 ULIRGs with $L_{\text{IR}} \geq 10^{12.3}L_{\odot}$ show strong buried AGN signatures, in contrast to only 11 out of 40 ULIRGs with $L_{\text{IR}} = 10^{12-12.3}L_{\odot}$ (Imanishi et al. 2007). When we combine these results, we obtain a fraction of strong buried AGN signatures of 18/25 (72%) for ULIRGs with $L_{\text{IR}} \geq 10^{12.3}L_{\odot}$ and 12/43 (28%) for ULIRGs with $L_{\text{IR}} = 10^{12-12.3}L_{\odot}$. When we include sources with *possible* buried AGN signatures (open triangles in Table 6 of this paper and Imanishi et al. 2007), the fraction of detectable buried AGNs signatures is 22/25 (88%) for ULIRGs with $L_{\text{IR}} \geq 10^{12.3}L_{\odot}$ and 19/43 (44%) for ULIRGs with $L_{\text{IR}} = 10^{12-12.3}L_{\odot}$. For optically non-Seyfert galaxies with $L_{\text{IR}} < 10^{12}L_{\odot}$, although the sample size is limited, no sources are classified as buried AGNs in our criteria (Figure 4). Other various observations also suggest that the energetic importance of buried AGNs clearly decreases in galaxies with $L_{\text{IR}} < 10^{12}L_{\odot}$, compared to ULIRGs (Soifer et al. 2000, 2001). Therefore, we clearly see the trend that *the detectable buried AGN fraction increases with infrared luminosity of optically non-Seyfert galaxies* (Figure 5), as has previously been suggested from *AKARI* infrared 2.5–

5 μm low-resolution spectroscopy (Imanishi et al. 2008). Given that the fraction of ULIRGs with optical Seyfert signatures also increases with increasing galaxy infrared luminosity (Veilleux et al. 1999; Goto 2005), we can conclude that *AGN activity becomes more important with increasing galaxy infrared luminosity*.

The so-called galaxy downsizing phenomenon has recently been proposed; it was found that galaxies with currently larger stellar masses finished their major star-formation in an earlier cosmic age (Cowie et al. 1996; Bundy et al. 2005). AGN feedback is suggested to be responsible for the galaxy downsizing phenomenon (Granato et al. 2004; Bower et al. 2006; Croton et al. 2006). Namely, in galaxies with currently large stellar masses, AGN feedback was stronger in the past, heating or expelling gas in host galaxies and stopping star formation on a shorter time scale. Buried AGNs can have particularly strong feedback because the AGNs are surrounded by a large amount of nuclear gas and dust. In addition, galaxies with currently larger stellar masses should have had higher star-formation-originating infrared luminosities in the past, as more stars were formed.

We found that the buried AGN fraction increases with increasing galaxy infrared luminosity. In ULIRGs with $L_{\text{IR}} > 10^{12}L_{\odot}$, the importance of buried AGNs suddenly becomes clear, compared to galaxies with $L_{\text{IR}} < 10^{12}L_{\odot}$ (Imanishi et al. 2007; this paper), suggesting that AGN feedback becomes significant in ULIRGs. The absorption-corrected intrinsic luminosities of detected buried AGNs are $>$ a few $\times 10^{45}$ ergs s^{-1} ($\gtrsim 10^{12}L_{\odot}$), which could account for a significant (15–100%) fraction of ULIRG infrared luminosities (Table 7 of this paper and Imanishi et al. 2007). The infrared luminosities of detected modestly-obscured starbursts (Table 7, columns 3 and 4) are also a few $\times 10^{45}$ ergs s^{-1} , or $\sim 10^{12}L_{\odot}$, which are still higher than the total infrared luminosities of galaxies with $L_{\text{IR}} < 10^{12}L_{\odot}$. Thus, both *stronger AGN feedback* and *higher star-formation-originating infrared luminosities* are suggested in ULIRGs³ than in lower L_{IR} galaxies.

Kauffmann et al. (2003) found that galaxies above and below stellar masses of $M_{*} = 3 \times 10^{10}M_{\odot}$ show distinctly different properties. Galaxies with $M_{*} > 3 \times 10^{10}M_{\odot}$ are dominated by red galaxies with currently low star-formation rates, while those with $M_{*} < 3 \times 10^{10}M_{\odot}$ are mainly blue galaxies with ongoing active star-formation. If AGN feedback is responsible for the dichotomy, then buried AGNs may become important in galaxies with $M_{*} > 3 \times 10^{10}M_{\odot}$. Based on the velocity dispersion measurements of ULIRG host galaxies in the infrared, Dasyra et al. (2006) argued that ULIRGs will have spheroidal stellar masses with several $\times 10^{10}M_{\odot}$. Assuming the Eddington luminosity for detected buried AGNs ($>$ a few

³ The summed luminosities of detected buried AGNs and modestly-obscured starbursts are generally smaller than the observed infrared luminosities of ULIRGs. This discrepancy may be due to (1) possible underestimation of absorption-corrected intrinsic buried AGN luminosity, caused by a small starburst contribution to the observed infrared flux (§5.2.7 of Imanishi et al. 2007), or by dust extinction curves in ULIRGs that differ from our assumption, or (2) the presence of highly dust-obscured ($A_{\text{V}} \gg 20$ mag) starbursts, or (3) intrinsically low PAH to infrared luminosity ratio in starburst activity in ULIRGs, or some combination of factors.

$\times 10^{45}$ ergs s^{-1}), SMBH masses are estimated to be a few $\times 10^7 M_{\odot}$. If we adopt the correlation between the masses of SMBH and spheroidal stars established in the local universe (Magorrian et al. 1998), similar spheroidal stellar masses with $>$ a few $\times 10^{10} M_{\odot}$ are obtained. These estimated spheroidal stellar masses of ULIRGs are similar to the value separating red massive (= strong AGN feedbacks) and blue, less-massive galaxies (= weak AGN feedbacks). In summary, our discovery of increasing buried AGN fraction with galaxy infrared luminosity may observationally support the widely-proposed AGN feedback scenario as the origin of the galaxy downsizing phenomenon.

6. SUMMARY

We presented the results of *Spitzer* IRS infrared 5–35 μm low-resolution spectroscopic energy diagnostic method of optically non-Seyfert ULIRGs at $z > 0.15$. The signatures of intrinsically luminous, but optically elusive, buried AGNs were searched for, based on the equivalent widths of PAH emission and the optical depths of silicate dust absorption features in these ULIRGs. Since most of the ULIRGs at $z > 0.15$ have $L_{\text{IR}} \geq 10^{12.3} L_{\odot}$, by combining results with our previous analysis of ULIRGs at $z < 0.15$, we could investigate the detectable buried AGN fraction by separating ULIRGs with $L_{\text{IR}} = 10^{12-12.3} L_{\odot}$ and $L_{\text{IR}} \geq 10^{12.3} L_{\odot}$. We found that the detectable buried AGN fraction is clearly higher in ULIRGs with $L_{\text{IR}} \geq 10^{12.3} L_{\odot}$ than those with L_{IR}

$= 10^{12-12.3} L_{\odot}$. Given that (1) the fraction of optical Seyferts is also higher in ULIRGs with $L_{\text{IR}} \geq 10^{12.3} L_{\odot}$ than in those with $L_{\text{IR}} = 10^{12-12.3} L_{\odot}$, and (2) signatures of AGNs, including both buried AGNs and optical Seyferts, are weaker in galaxies with $L_{\text{IR}} < 10^{12} L_{\odot}$ than ULIRGs, we concluded that AGN importance increases as galaxy infrared luminosity increases. Buried AGNs become clearly discernible in ULIRGs with implied stellar masses of $M_{*} >$ a few $\times 10^{10} M_{\odot}$, the value that separates red massive and blue, less-massive galaxies in the nearby universe. Our overall results support the AGN-feedback scenario as the origin of the galaxy downsizing phenomenon.

We thank the anonymous referee for his/her very useful comments. This work is based on observations made with the Spitzer Space Telescope, operated by the Jet Propulsion Laboratory, California Institute of Technology under a contract with NASA. Support for this work was provided by NASA and also by an award issued by JPL/Caltech. M.I. is supported by Grants-in-Aid for Scientific Research (19740109). This research made use of the SIMBAD database, operated at CDS, Strasbourg, France, and the NASA/IPAC Extragalactic Database (NED), which is operated by the Jet Propulsion Laboratory, California Institute of Technology, under contract with NASA.

REFERENCES

- Bower, R. G., Benson, A. J., Malbon, R., Helly, J. C., Frenk, C. S., Baugh, C. M., Cole, S., & Lacey, C. G. 2006, MNRAS, 370, 645
- Brandl, B. R., et al. 2006, ApJ, 653, 1129
- Bundy, K., Ellis, R. S., & Conselice, C. J. 2005, ApJ, 625, 621
- Caputi, K. I., et al. 2007, ApJ, 660, 97
- Cowie, L. L., Songaila, A., Hu, E. M., & Cohen, J. G. 1996, AJ, 112, 839
- Croton, D. J., et al. 2006, MNRAS, 365, 11
- Dasyra, K. M., et al. 2006, ApJ, 651, 835
- Dudley, C. C., & Wynn-Williams, C. G. 1997, ApJ, 488, 720
- Farrah, D. et al. 2007, ApJ, 667, 149
- Forster Schreiber, N. M., Genzel, R., Lutz, D., Kunze, D., & Sternberg, A. 2001, ApJ, 552, 544
- Houck, J. R., et al. 2004, ApJS, 154, 18
- Genzel, R. et al. 1998, ApJ, 498, 579
- Goto, T. 2005, MNRAS, 360, 322
- Granato, G. L., De Zotti, G., Silva, L., Bressan, A., & Danese, L. 2004, ApJ, 600, 580
- Imanishi, M. 2000, MNRAS, 319, 331
- Imanishi, M., & Dudley, C. C. 2000, ApJ, 545, 701
- Imanishi, M., & Maloney, P. R. 2003, ApJ, 588, 165
- Imanishi, M., Dudley, C. C., & Maloney, P. R. 2006, ApJ, 637, 114
- Imanishi, M., Dudley, C. C., Maiolino, R., Maloney, P. R., Nakagawa, T., & Risaliti, G. 2007, ApJS, 171, 72
- Imanishi, M., Nakagawa, T., Ohyama, Y., Shirahata, M., Wada, T., Onaka, T., & Oi, N. 2008, PASJ, in press (ArXiv:0808:0363)
- Kauffmann, G., et al. 2003, MNRAS, 341, 54
- Kewley, L. J., Groves, B., Kauffmann, G., & Heckman, T. 2006, MNRAS, 372, 961
- Kim, D. -C., & Sanders, D. B., 1998, ApJS, 119, 41
- Le Floc'h et al. 2005, ApJ, 632, 169
- Levenson, N. A., Sirocky, M. M., Hao, L., Spoon, H. W. W., Marshall, J. A., Elitzur, M., & Houck, J. R., 2007, ApJ, 654, L45
- Lutz, D. et al. 1996, A&A, 315, L269
- Magorrian, J., et al. 1998, ApJ, 115, 2285
- McLeod, K. K., Rieke, G. H., Rieke, M. J., & Kelly, D. M. 1993, ApJ, 412, 111
- Peeters, E., Spoon, H. W. W., & Tielens, A. G. G. M. 2004, ApJ, 613, 986
- Perez-Gonzalez, P. G., et al. 2005, ApJ, 630, 82
- Puxley, P. J. 1991, MNRAS, 249, 11p
- Rieke, G. H., & Lebofsky, M. J. 1985, ApJ, 288, 618
- Sanders, D. B., & Mirabel, I. F. 1996, ARA&A, 34, 749
- Sanders, D. B., Soifer, B. T., Elias, J. H., Madore, B. F., Matthews, K., Neugebauer, G., & Scoville, N. Z. 1988a, ApJ, 325, 74
- Sanders, D. B., Soifer, B. T., Elias, J. H., Neugebauer, G., & Matthews, K. 1988b, ApJ, 328, L35
- Sellgren, K. 1981, ApJ, 245, 138
- Siebenmorgen, R., Krugel, E., & Spoon, H. W. W. 2004, A&A, 414, 123
- Sirocky, M. M., Levenson, N. A., Elitzur, M., Spoon, H. W. W., & Armus, L. 2008, ApJ, 678, 729
- Soifer, B. T. et al. 2000, AJ, 119, 509
- Soifer, B. T. et al. 2001, AJ, 122, 1213
- Soifer, B. T., Neugebauer, G., Matthews, K., Egami, E., & Weinberger, A. J. 2002, AJ, 124, 2980
- Veilleux, S., Kim, D. -C., & Sanders, D. B. 1999, ApJ, 522, 113
- Veilleux, S., & Osterbrock, D. E. 1987, ApJS, 63, 295
- Voit, G. M. 1992, MNRAS, 258, 841
- Werner, M. W., et al. 2004, ApJS, 154, 1
- Wu, Y., Charmandaris, V., Hao, L., Brandl, B. R., Bernard-Salas, J., Spoon, H. W. W., & Houck, J. R. 2006, ApJ, 639, 157

TABLE 1
OBSERVED ULIRGS AT $z > 0.15$ AND THEIR *IRAS*-BASED INFRARED EMISSION PROPERTIES

Object	Redshift	f_{12} (Jy)	f_{25} (Jy)	f_{60} (Jy)	f_{100} (Jy)	$\log L_{\text{IR}}$ L_{\odot}	f_{25}/f_{60}	Optical Class
(1)	(2)	(3)	(4)	(5)	(6)	(7)	(8)	(9)
IRAS 03521+0028	0.152	<0.11	0.20	2.52	3.62	12.5	0.08 (C)	LINER
IRAS 09463+8141	0.156	<0.07	<0.07	1.43	2.29	12.3	<0.05 (C)	LINER
IRAS 10091+4704	0.246	<0.06	<0.08	1.18	1.55	12.6	<0.07 (C)	LINER
IRAS 11028+3130	0.199	<0.09	0.09	1.02	1.44	12.4	0.09 (C)	LINER
IRAS 11180+1623	0.166	<0.08	<0.19	1.19	1.60	12.2	<0.16 (C)	LINER
IRAS 11582+3020	0.223	<0.10	<0.15	1.13	1.49	12.5	<0.14 (C)	LINER
IRAS 12032+1707	0.217	<0.14	0.25	1.36	1.54	12.6	0.18 (C)	LINER
IRAS 16300+1558	0.242	<0.07	0.07	1.48	1.99	12.7	0.05 (C)	LINER
IRAS 16333+4630	0.191	<0.06	0.06	1.19	2.09	12.4	0.05 (C)	LINER
IRAS 23129+2548	0.179	<0.08	0.08	1.81	1.64	12.4	0.04 (C)	LINER
IRAS 00397-1312	0.261	0.14	0.33	1.83	1.90	12.9	0.18 (C)	HII-region
IRAS 01199-2307	0.156	<0.11	<0.16	1.61	1.37	12.3	<0.1 (C)	HII-region
IRAS 01355-1814	0.192	<0.06	0.12	1.40	1.74	12.4	0.09 (C)	HII-region
IRAS 08201+2801	0.168	<0.09	0.15	1.17	1.43	12.3	0.13 (C)	HII-region
IRAS 13469+5833	0.158	<0.05	0.04	1.27	1.73	12.2	0.03 (C)	HII-region
IRAS 17068+4027	0.179	<0.08	0.12	1.33	1.41	12.3	0.09 (C)	HII-region
IRAS 01494-1845	0.158	<0.08	<0.15	1.29	1.85	12.2	<0.12 (C)	unclassified
IRAS 04313-1649	0.268	<0.07	0.07	1.01	1.10	12.6	0.07 (C)	unclassified
IRAS 10035+2740	0.165	<0.14	<0.17	1.14	1.63	12.3	<0.15 (C)	unclassified
IRAS 12018+1941	0.168	<0.11	0.37	1.76	1.78	12.5	0.21 (W)	unclassified

NOTE. — Col.(1): Object name. Col.(2): Redshift. Col.(3)–(6): f_{12} , f_{25} , f_{60} , and f_{100} are *IRAS* fluxes at 12 μm , 25 μm , 60 μm , and 100 μm , respectively, taken from Kim & Sanders (1998). Col.(7): Decimal logarithm of infrared (8–1000 μm) luminosity in units of solar luminosity (L_{\odot}), calculated with $L_{\text{IR}} = 2.1 \times 10^{39} \times D(\text{Mpc})^2 \times (13.48 \times f_{12} + 5.16 \times f_{25} + 2.58 \times f_{60} + f_{100}) \text{ ergs s}^{-1}$ (Sanders & Mirabel 1996). Since the calculation is based on our adopted cosmology, the infrared luminosities differ slightly (<10%) from the values shown in Kim & Sanders (1998, Table 1, column 15). For sources with upper limits in some *IRAS* bands, we can derive upper and lower limits for infrared luminosity, assuming that the actual flux is the *IRAS*-upper limit and zero value, respectively. The difference in the upper and lower values is usually very small, less than 0.2 dex. We assume that the infrared luminosity is the average of these values. Col.(8): *IRAS* 25 μm to 60 μm flux ratio. ULIRGs with $f_{25}/f_{60} < 0.2$ and > 0.2 are classified as cool and warm sources (denoted as “C” and “W”), respectively (Sanders et al. 1988b). Col.(9): Optical spectral classification by Veilleux et al. (1999).

TABLE 2
Spitzer IRS OBSERVING LOG

Object	PID	Date [UT]	Integration time [sec]			
			SL2 (4)	SL1 (5)	LL2 (6)	LL1 (7)
(1)	(2)	(3)	(4)	(5)	(6)	(7)
IRAS 03521+0028	105	2004 Feb 27	240	240	180	180
IRAS 09463+8141	105	2004 Mar 23	240	240	120	120
IRAS 10091+4704	105	2004 Apr 19	240	240	120	120
IRAS 11028+3130	30407	2007 Jun 9	240	240	180	180
IRAS 11180+1623	30407	2007 Jun 8	196	196	180	180
IRAS 11582+3020	105	2005 Dec 16	240	240	120	120
IRAS 12032+1707	105	2004 Jan 4	240	240	120	120
IRAS 16300+1558	105	2005 Aug 13	240	240	300	300
IRAS 16333+4630	105	2004 Mar 4	240	240	120	120
IRAS 23129+2548	105	2003 Dec 17	360	360	300	300
IRAS 00397-1312	105	2004 Jan 4	240	240	180	180
IRAS 01199-2307	105	2004 Jul 18	240	240	180	180
IRAS 01355-1814	105	2005 Jul 10	240	240	120	120
IRAS 08201+2801	30407	2007 May 3	196	196	180	180
IRAS 13469+5833	20589	2006 Apr 26	240	112	480	960
IRAS 17068+4027	105	2004 Apr 16	240	240	180	180
IRAS 01494-1845	105	2005 Jul 14	240	240	120	120
IRAS 04313-1649	105	2004 Mar 1	240	240	300	300
IRAS 10035+2740	30407	2007 Jun 8	196	196	180	180
IRAS 12018+1941	105	2004 May 15	120	120	180	180

NOTE. — Col.(1): Object name. Col.(2): PID number. Col.(3): Observing date in UT. Col.(4): Net on-source integration time for SL2 spectroscopy in sec. Col.(5): Net on-source integration time for SL1 spectroscopy in sec. Col.(6): Net on-source integration time for LL2 spectroscopy in sec. Col.(7): Net on-source integration time for LL1 spectroscopy in sec.

TABLE 3
OBSERVED PROPERTIES OF PAH EMISSION FEATURES

Object	EW _{6.2PAH}	EW _{7.7PAH} ^a	EW _{11.3PAH}	L _{6.2PAH}	L _{7.7PAH} ^a	L _{11.3PAH}	L _{6.2PAH} /L _{IR}	L _{11.3PAH} /L _{IR}
(1)	[nm] (2)	[nm] (3)	[nm] (4)	10 ⁴² [ergs s ⁻¹] (5)	10 ⁴² [ergs s ⁻¹] (6)	10 ⁴² [ergs s ⁻¹] (7)	[× 10 ⁻³] (8)	[× 10 ⁻³] (9)
IRAS 03521+0028	245	855	450	6.1	24.3	5.2	0.5	0.4
IRAS 09463+8141	225	765	530	2.9	11.3	1.7	0.4	0.3
IRAS 10091+4704	<50	480	560	<1.7	29.1	3.5	<0.2	0.2
IRAS 11028+3130	160	870	460	1.9	12.1	1.7	0.2	0.2
IRAS 11180+1623	165	855	340	4.1	25.6	2.7	0.6	0.4
IRAS 11582+3020	70	235	325	6.4	63.1	5.9	0.5	0.5
IRAS 12032+1707	70	195	315	5.2	26.1	5.9	0.3	0.4
IRAS 16300+1558	85	410	400	7.4	40.6	6.0	0.4	0.3
IRAS 16333+4630	275	680	485	13.1	42.6	11.6	1.4	1.2
IRAS 23129+2548	110	320	330	5.9	30.8	4.1	0.6	0.4
IRAS 00397-1312	25	160	35	21.4	135.5	2.9	0.6	0.09
IRAS 01199-2307	130	440	215	4.3	21.8	1.9	0.6	0.3
IRAS 01355-1814	170	605	195	4.2	19.1	1.7	0.4	0.2
IRAS 08201+2801	105	425	280	5.5	33.8	4.2	0.8	0.6
IRAS 13469+5833	235	675	460	4.0	15.7	3.4	0.7	0.6
IRAS 17068+4027	110	405	185	8.5	40.1	5.0	1.0	0.6
IRAS 01494-1845	365	810	485	8.0	25.0	5.0	1.3	0.8
IRAS 04313-1649	<120	305	240	<3.2	15.3	2.1	<0.3	0.1
IRAS 10035+2740	660	900	275	5.0	9.8	1.1	0.8	0.2
IRAS 12018+1941	120	220	35	9.3	24.5	2.3	0.9	0.2

NOTE. — Col.(1): Object name. Col.(2): Rest-frame equivalent width of the 6.2 μm PAH emission. Col.(3): Rest-frame equivalent width of the 7.7 μm PAH emission. Col.(4): Rest-frame equivalent width of the 11.3 μm PAH emission. Col.(5): Luminosity of the 6.2 μm PAH emission in units of 10^{42} ergs s⁻¹. Col.(6): Luminosity of the 7.7 μm PAH emission in units of 10^{42} ergs s⁻¹. Col.(7): Luminosity of the 11.3 μm PAH emission in units of 10^{42} ergs s⁻¹. Col.(8): The 6.2 μm PAH to infrared luminosity ratio in units of 10^{-3} . The ratio for normal starbursts with modest dust obscuration ($A_V < 20$ mag) is $\sim 3.4 \times 10^{-3}$ (Peeters et al. 2004). Col.(9): The 11.3 μm PAH to infrared luminosity ratio in units of 10^{-3} . The ratio for normal starbursts with modest dust obscuration ($A_V < 20$ mag) is $\sim 1.4 \times 10^{-3}$ (Soifer et al. 2002).

^aWe regard flux excess at $\lambda_{\text{rest}} = 7.3\text{--}8.1$ μm above an adopted continuum level as 7.7 μm PAH emission, to reduce the effects of the strong 9.7 μm silicate dust absorption feature. Our definition is different from those presented in previous papers.

TABLE 4
9.7 μM AND 18 μM SILICATE DUST
ABSORPTION FEATURE OPTICAL DEPTHS

Object (1)	$\tau'_{9.7}$ (2)	τ'_{18} (3)	$\tau'_{18}/\tau'_{9.7}$ (4)
IRAS 03521+0028	1.3	0.4	0.31
IRAS 09463+8141	2.0	0.6	0.30
IRAS 10091+4704	2.5	1.0	0.40
IRAS 11028+3130	2.5	1.1	0.44
IRAS 11180+1623	2.0	0.6	0.30
IRAS 11582+3020	2.7	0.8	0.30
IRAS 12032+1707	2.6	0.6	0.23
IRAS 16300+1558	2.6	0.9	0.35
IRAS 16333+4630	1.3
IRAS 23129+2548	2.6	0.9	0.35
IRAS 00397-1312	2.7	0.6	0.22
IRAS 01199-2307	2.4	0.7	0.29
IRAS 01355-1814	2.4	0.7	0.29
IRAS 08201+2801	2.2	0.5	0.23
IRAS 13469+5833	1.7	0.5	0.29
IRAS 17068+4027	1.8	0.5	0.28
IRAS 01494-1845	1.6
IRAS 04313-1649	2.8	0.7	0.25
IRAS 10035+2740	2.0	0.7	0.35
IRAS 12018+1941	1.3	0.3	0.23

NOTE. — Col.(1): Object name. Col.(2): $\tau'_{9.7}$ is optical depth of the 9.7 μm silicate dust absorption feature, against a power-law continuum shown as dotted lines in Figure 1. Once the continuum levels are fixed, the uncertainty of $\tau'_{9.7}$ is $<5\%$ for ULIRGs with large $\tau'_{9.7}$ values (>2) and can be $\sim 10\%$ for ULIRGs with small $\tau'_{9.7}$. Col.(3): τ'_{18} is optical depth of the 18 μm silicate dust absorption feature, against a power-law continuum shown as dotted lines in Figure 1. Once the continuum is fixed, the uncertainty of τ'_{18} is $<10\%$ because the value is estimated only for ULIRGs with clearly detectable 18 μm silicate absorption features. Col.(4): $\tau'_{18}/\tau'_{9.7}$ ratio for ULIRGs with clearly detectable 18 μm silicate absorption.

TABLE 5
ICE AND CO ABSORPTION FEATURES

Object (1)	$\tau_{6.0}$ (2)	τ_{CO} (3)
IRAS 09463+8141	0.7	...
IRAS 11582+3020	0.3	...
IRAS 12032+1707	0.5	...
IRAS 16300+1558	0.3	...
IRAS 16333+4630	0.4	...
IRAS 23129+2548	0.4	...
IRAS 00397-1312	0.2	1.0 (P), 1.2 (R)
IRAS 01355-1814	0.3	...
IRAS 08201+2801	0.5	...
IRAS 13469+5833	0.9	...
IRAS 17068+4027	0.3	...

NOTE. — Col.(1): Object name. Col.(2): Optical depth of the 6.0 μm H₂O ice absorption feature for clearly detected sources. Col.(3): Optical depth of the 4.67 μm CO absorption feature. “P” means the P-branch of the CO absorption feature (the sub-peak at longer wavelength). “R” means the R-branch of the CO absorption feature (the sub-peak at shorter wavelength).

TABLE 6
BURIED AGN SIGNATURES

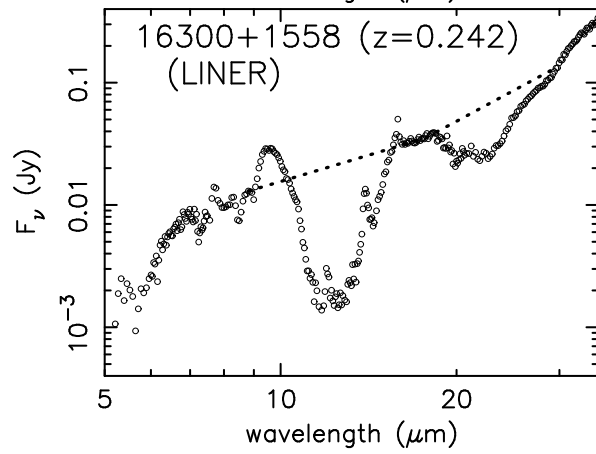
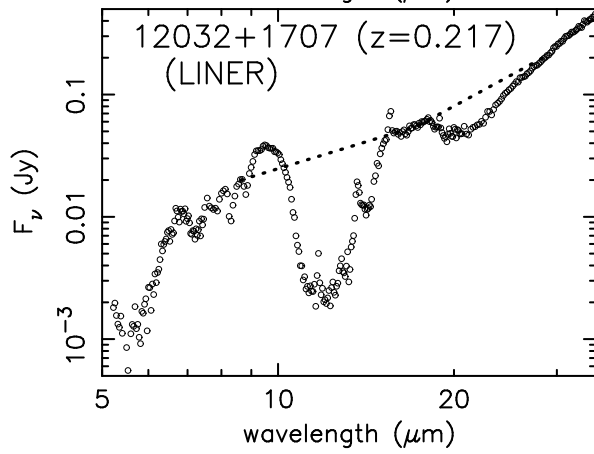
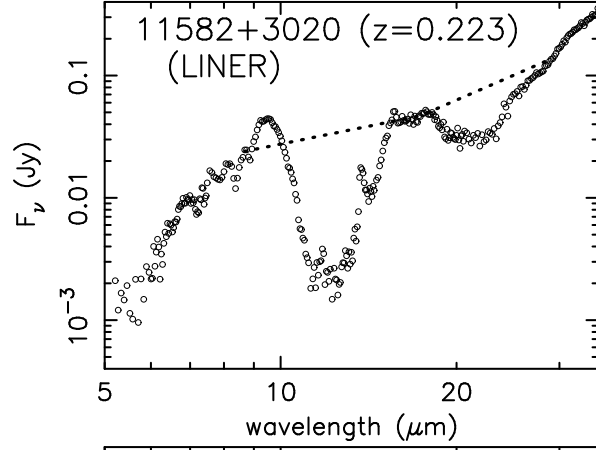
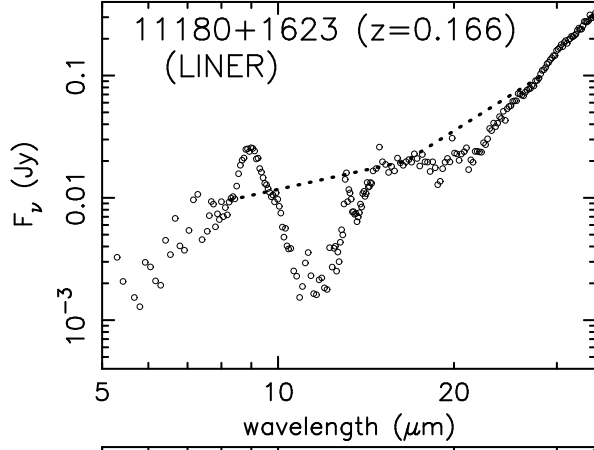
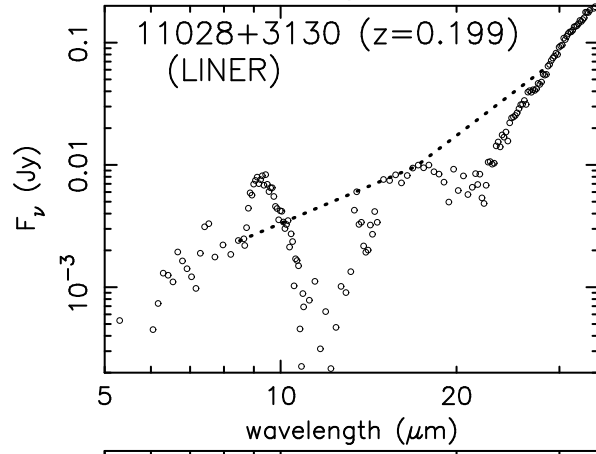
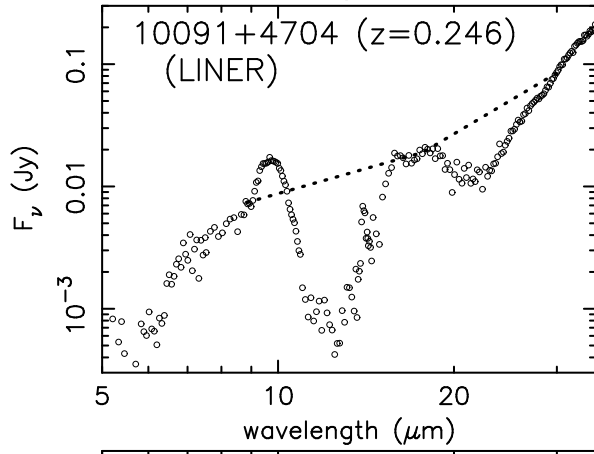
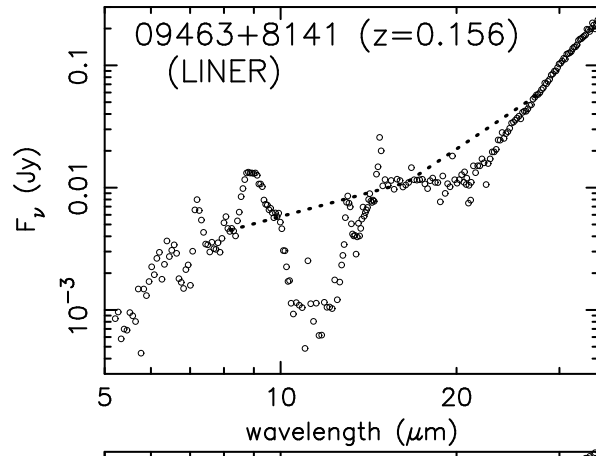
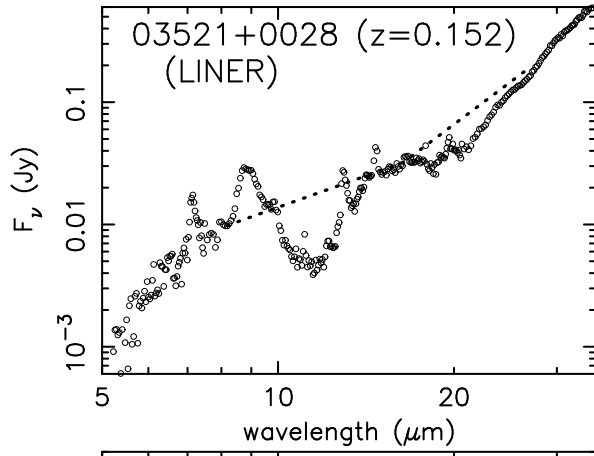
Object (1)	EW _{6.2PAH} (2)	EW _{7.7PAH} (3)	EW _{11.3PAH} (4)	$\tau'_{9.7}$ (5)	T-gradient (6)	Total (7)
IRAS 03521+0028	X	X	X	X	X	X
IRAS 09463+8141	X	X	X	○	X	△
IRAS 10091+4704	○	X	X	○	X	○
IRAS 11028+3130	○	X	X	○	X	○
IRAS 11180+1623	○	X	X	○	X	○
IRAS 11582+3020	○	X	X	○	X	○
IRAS 12032+1707	○	○	X	○	○	⊙
IRAS 16300+1558	○	X	X	○	X	○
IRAS 16333+4630	X	X	X	X	X	X
IRAS 23129+2548	○	X	X	○	X	○
IRAS 00397-1312	○	○	○	○	○	⊙
IRAS 01199-2307	○	X	X	○	X	○
IRAS 01355-1814	○	X	○	○	X	○
IRAS 08201+2801	○	X	X	○	○	⊙
IRAS 13469+5833	X	X	X	X	X	X
IRAS 17068+4027	○	X	○	X	X	○
IRAS 01494-1845	X	X	X	X	X	X
IRAS 04313-1649	○	X	X	○	○	⊙
IRAS 10035+2740	X	X	X	○	X	△
IRAS 12018+1941	○	○	○	X	○	⊙

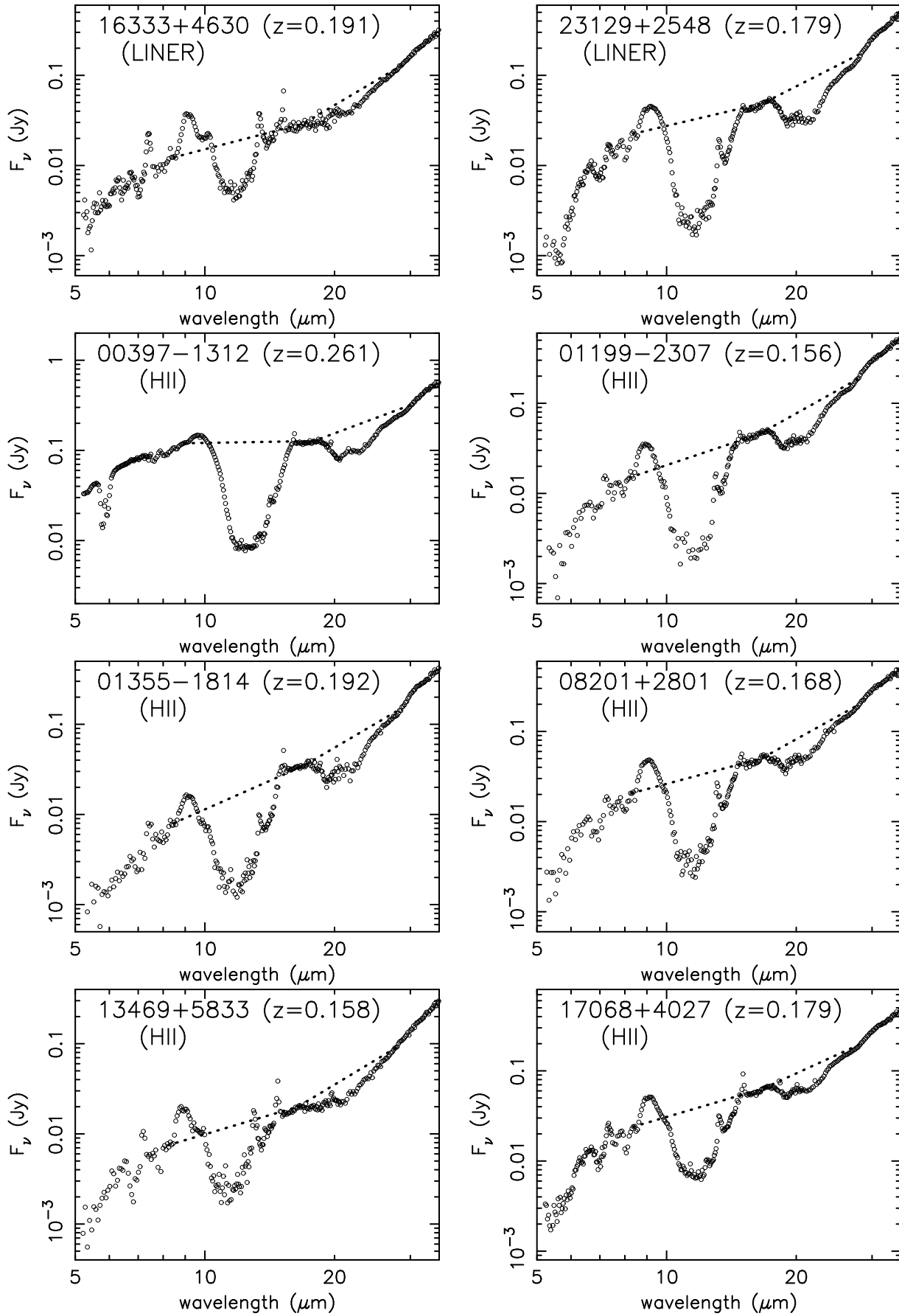
NOTE. — Col.(1): Object name. Col.(2): Buried AGN signatures based on the low equivalent width of the 6.2 μm PAH emission ($\text{EW}_{6.2\text{PAH}} < 180 \text{ nm}$) (§5.2.1). ○: present. X: none. Col.(3): Buried AGN signatures based on the low equivalent width of the 7.7 μm PAH emission ($\text{EW}_{7.7\text{PAH}} < 230 \text{ nm}$) (§5.2.1). ○: present. X: none. Col.(4): Buried AGN signatures based on the low equivalent width of the 11.3 μm PAH emission ($\text{EW}_{11.3\text{PAH}} < 200 \text{ nm}$) (§5.2.1). ○: present. X: none. Col.(5): Buried AGN signatures based on the large $\tau'_{9.7}$ value (> 2) (§5.2.2). ○: present. X: none. Col.(6): Buried AGN signatures based on the small $\tau'_{18}/\tau'_{9.7}$ ratio (§5.2.3). ○: present. X: none. Col.(7): Buried AGN signatures from combined methods in Col. (2)–(6). ⊙: very strong. ○: strong. △: possible. X: none. Please see §5.2.4 for more details.

TABLE 7
ABSORPTION-CORRECTED AGN LUMINOSITY

Object (1)	L(AGN) $10^{45} [\text{ergs s}^{-1}]$ (2)	L(SB-6.2PAH) $10^{45} [\text{ergs s}^{-1}]$ (3)	L(SB-11.3PAH) $10^{45} [\text{ergs s}^{-1}]$ (4)	L _{IR} $10^{45} [\text{ergs s}^{-1}]$ (5)
IRAS 10091+4704	2	<0.5	2.5	15
IRAS 11582+3020	4	1.9	4.2	12
IRAS 12032+1707	3.5	1.5	4.2	15
IRAS 16300+1558	3	2.2	4.3	18
IRAS 00397-1312	20	6.3	2.0	34
IRAS 17068+4027	2	2.5	3.6	8
IRAS 04313-1649	2	<1.0	1.5	15
IRAS 12018+1941	2	2.7	1.7	11

NOTE. — Col.(1): Object name. Col.(2): Absorption-corrected intrinsic luminosity of buried AGN in units of $10^{45} \text{ ergs s}^{-1}$. Col.(3): Infrared (8–1000 μm) luminosity of detected modestly-obscured ($A_V < 20 \text{ mag}$) starbursts, estimated from the 6.2 μm PAH emission luminosity, in units of $10^{45} \text{ ergs s}^{-1}$. Col.(4): Infrared (8–1000 μm) luminosity of detected modestly-obscured ($A_V < 20 \text{ mag}$) starbursts, estimated from the 11.3 μm PAH emission luminosity, in units of $10^{45} \text{ ergs s}^{-1}$. Col.(5): Observed infrared luminosity in units of $10^{45} \text{ ergs s}^{-1}$.





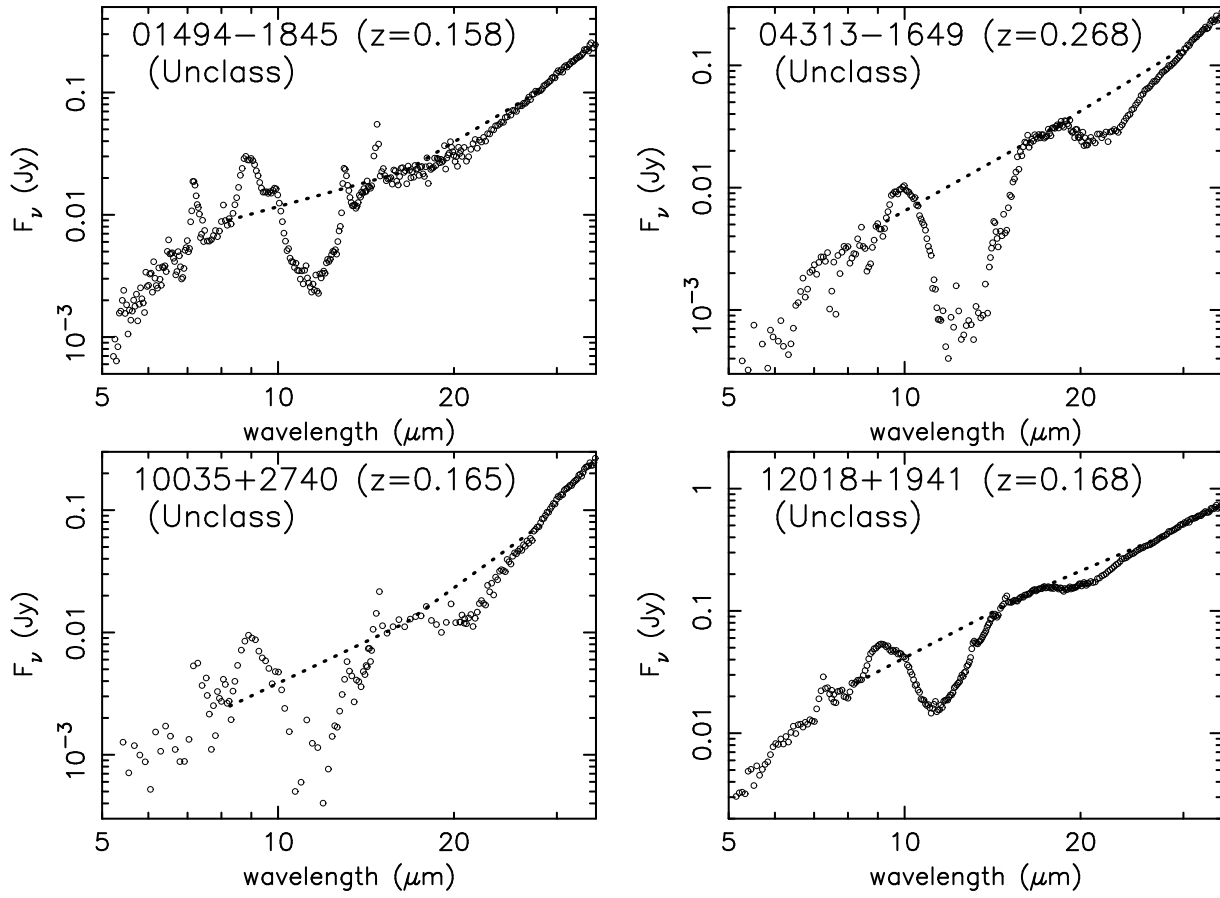
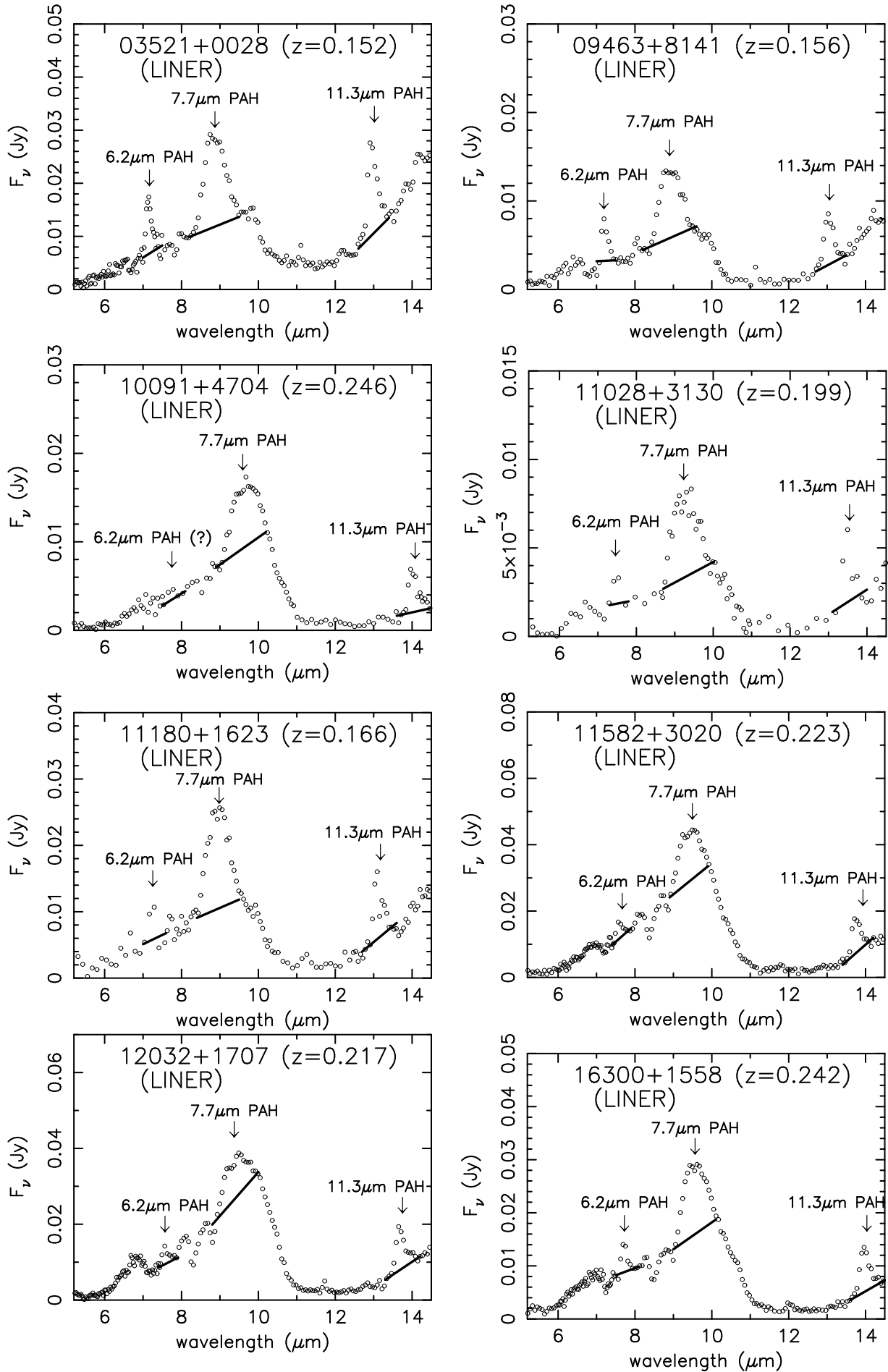
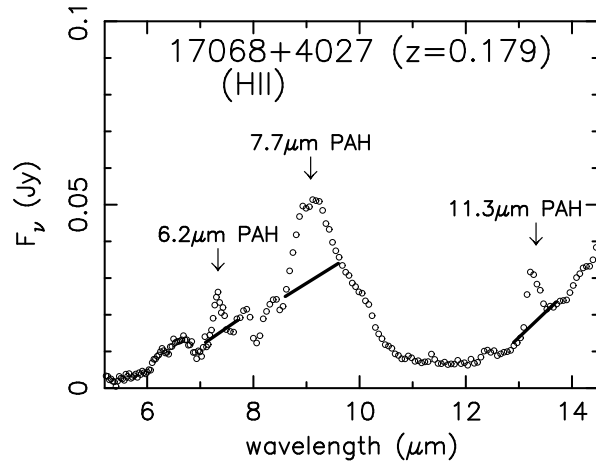
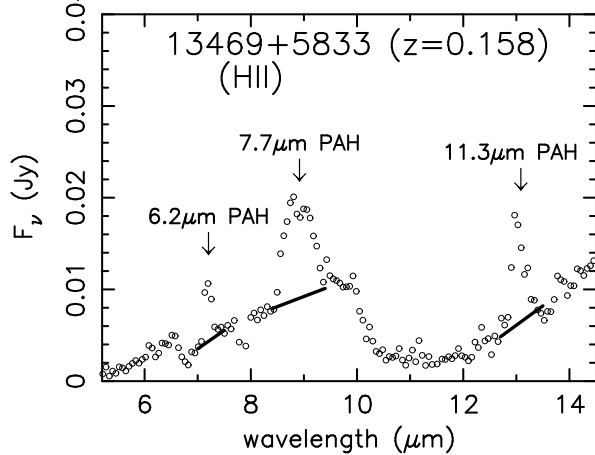
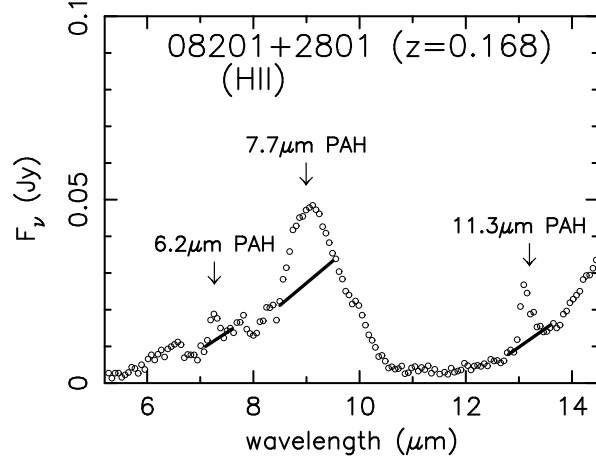
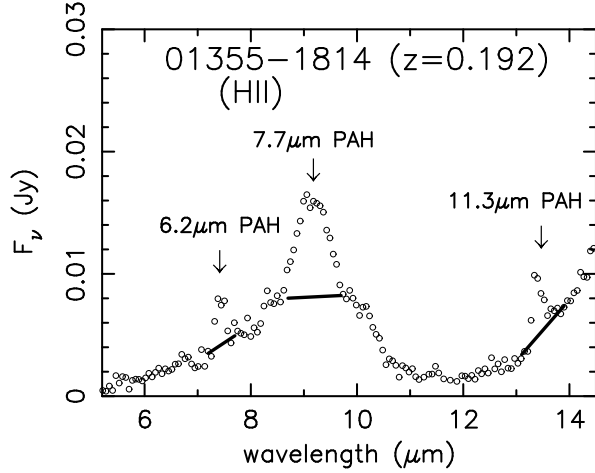
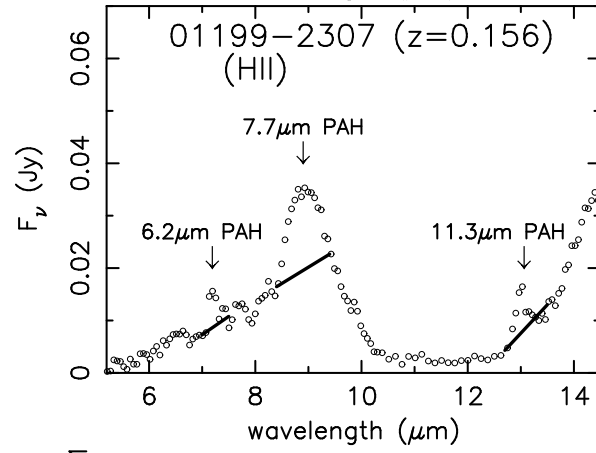
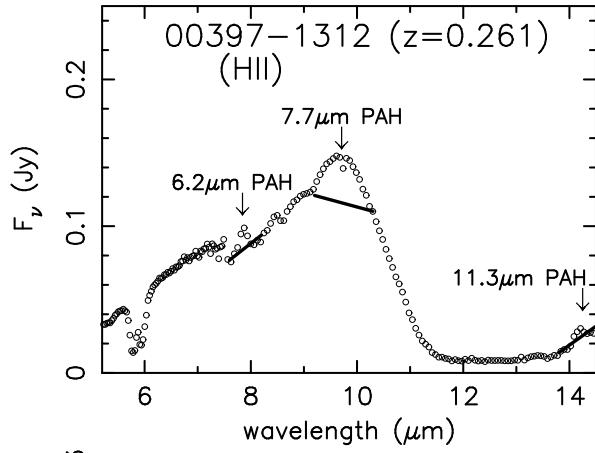
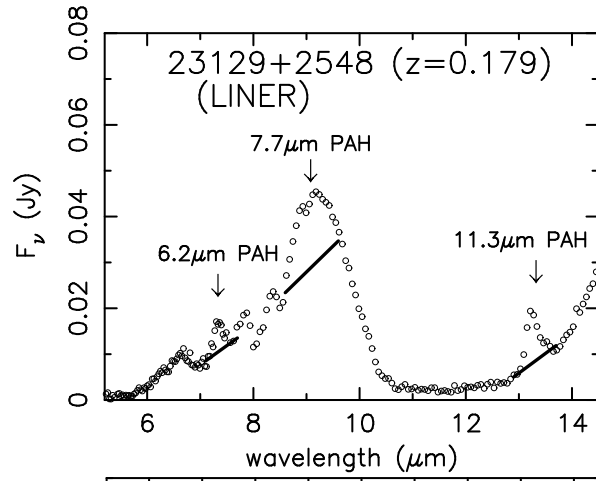
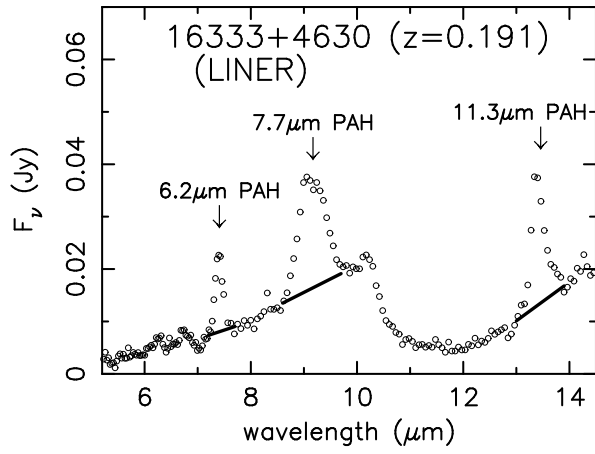


FIG. 1.— Infrared 5–35 μm ULIRG spectra obtained with *Spitzer* IRS. The abscissa and ordinate are, respectively, the observed wavelength in μm and flux F_ν in Jy, both shown in decimal logarithmic scale. For all objects, the ratio of the uppermost to lowermost scale in the ordinate is a factor of 1000, showing the variation of overall spectral energy distribution. Dotted line: power-law continuum determined from data points at $\lambda_{\text{rest}} = 7.1 \mu\text{m}$ and $14.2 \mu\text{m}$ for $9.7 \mu\text{m}$ silicate absorption, and at $\lambda_{\text{rest}} = 14.2 \mu\text{m}$ and $24 \mu\text{m}$ for $18 \mu\text{m}$ silicate absorption.





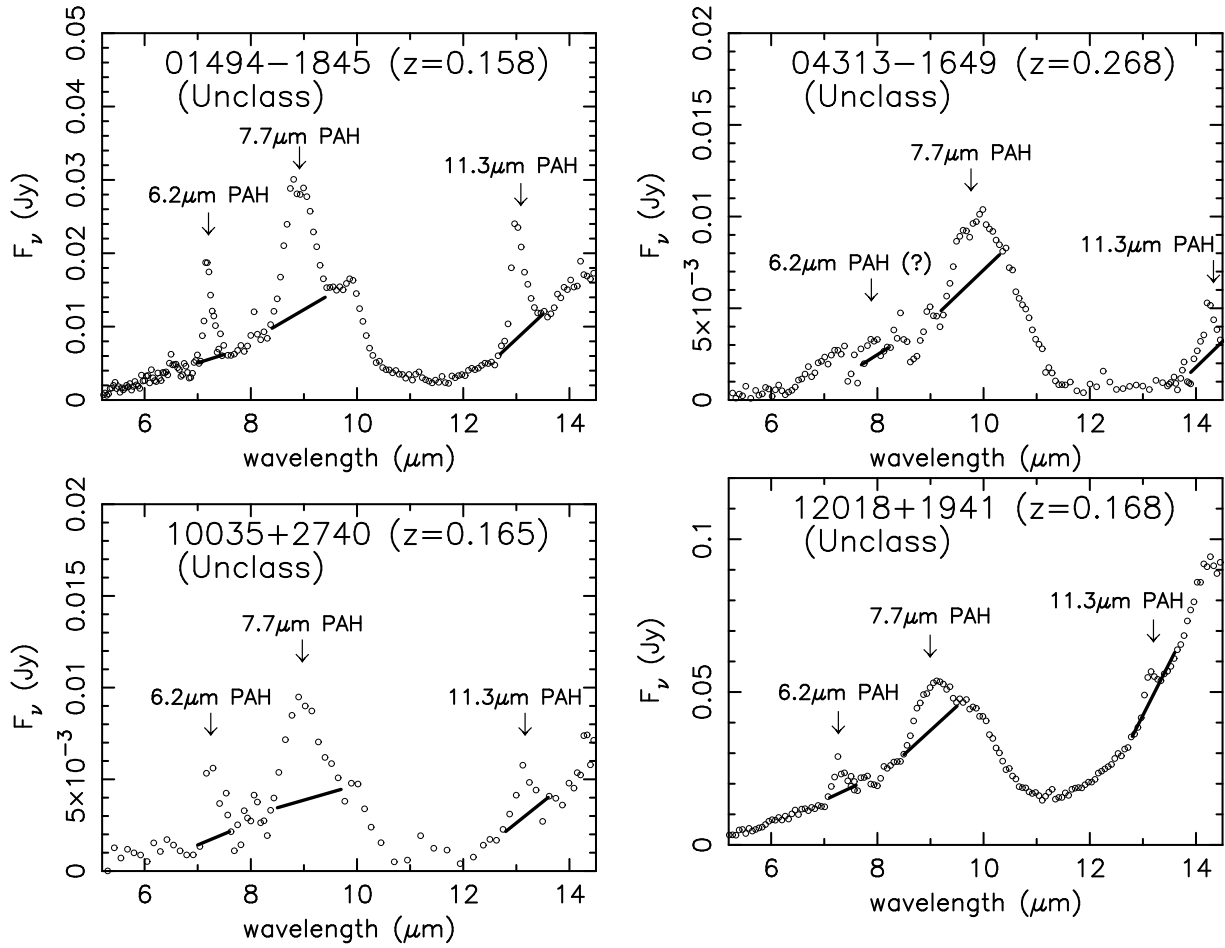
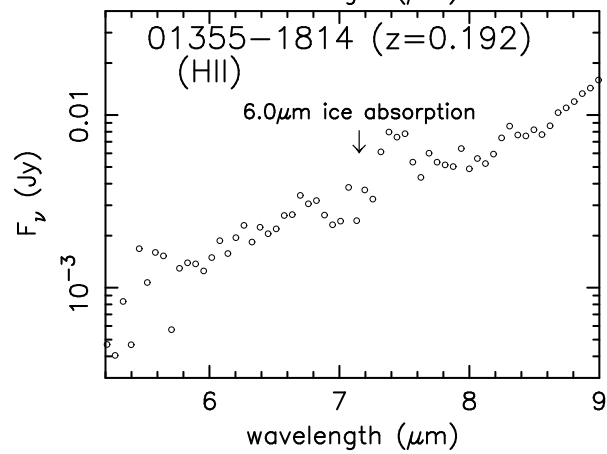
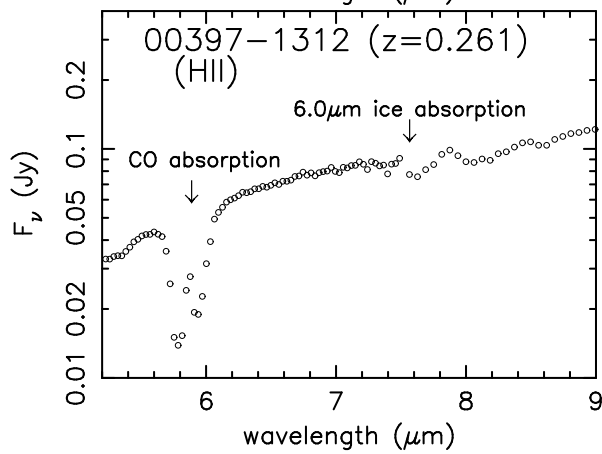
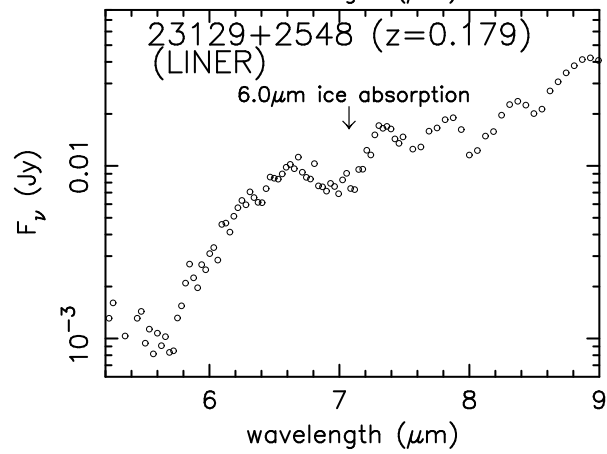
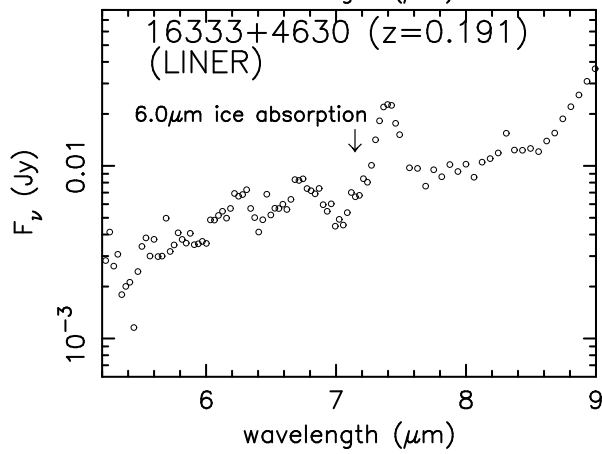
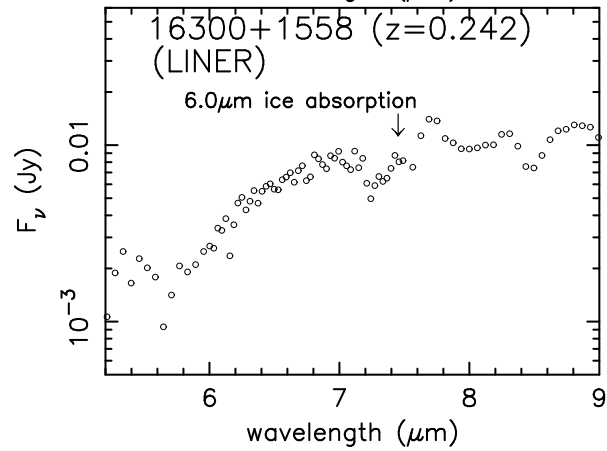
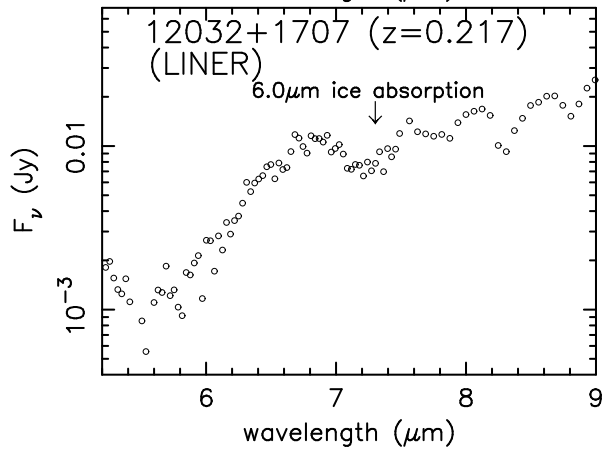
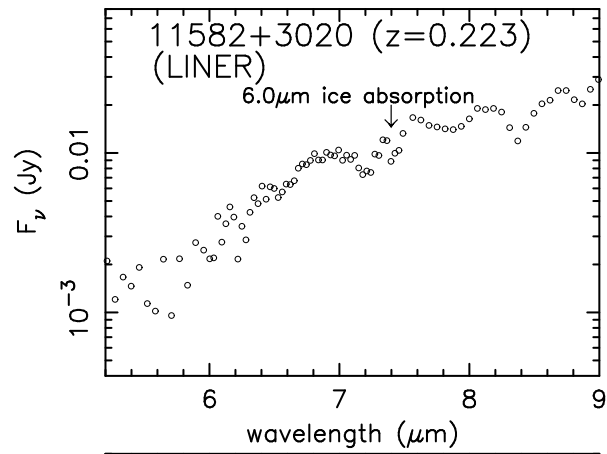
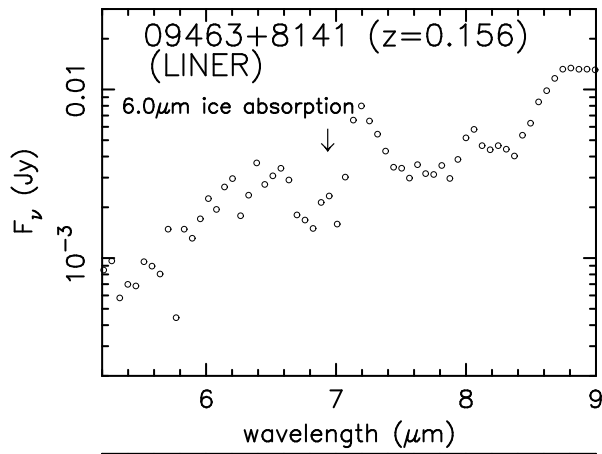


FIG. 2.— *Spitzer* IRS spectra of all ULIRGs at $\lambda_{\text{obs}} = 5.2\text{--}14.5 \mu\text{m}$, selected to display the PAH emission features in detail. The abscissa and ordinate are, respectively, observed wavelength in μm and flux in Jy, both shown on a linear scale. The expected wavelengths of the 6.2 μm , 7.7 μm , and 11.3 μm PAH emission features are indicated as down arrows. The mark “(?)” is added when detection is unclear. The solid lines are adopted continuum levels to estimate the strengths of the PAH emission features.



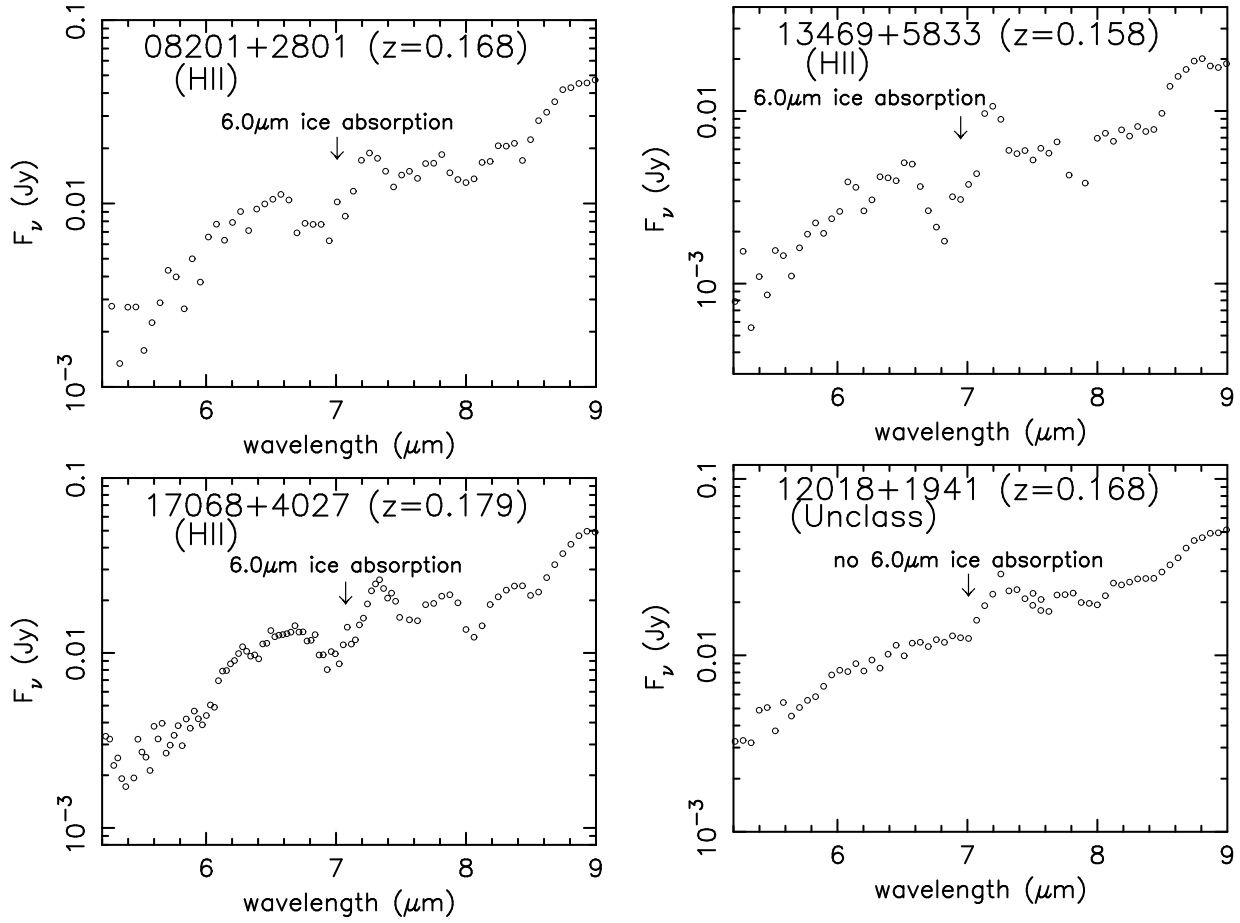


FIG. 3.— *Spitzer* IRS spectra at $\lambda_{\text{obs}} = 5.2\text{--}9\ \mu\text{m}$ for ULIRGs displaying clear $6.0\ \mu\text{m}$ H_2O ice absorption features (marked with “ $6.0\ \mu\text{m}$ ice absorption” in the first 11 plots). The spectrum of IRAS 12018+1941, marked “no $6.0\ \mu\text{m}$ ice absorption”, is shown as an example of an undetected ice absorption feature. The abscissa is observed wavelength in μm on a linear scale, and the ordinate is flux in Jy in decimal logarithmic scale.

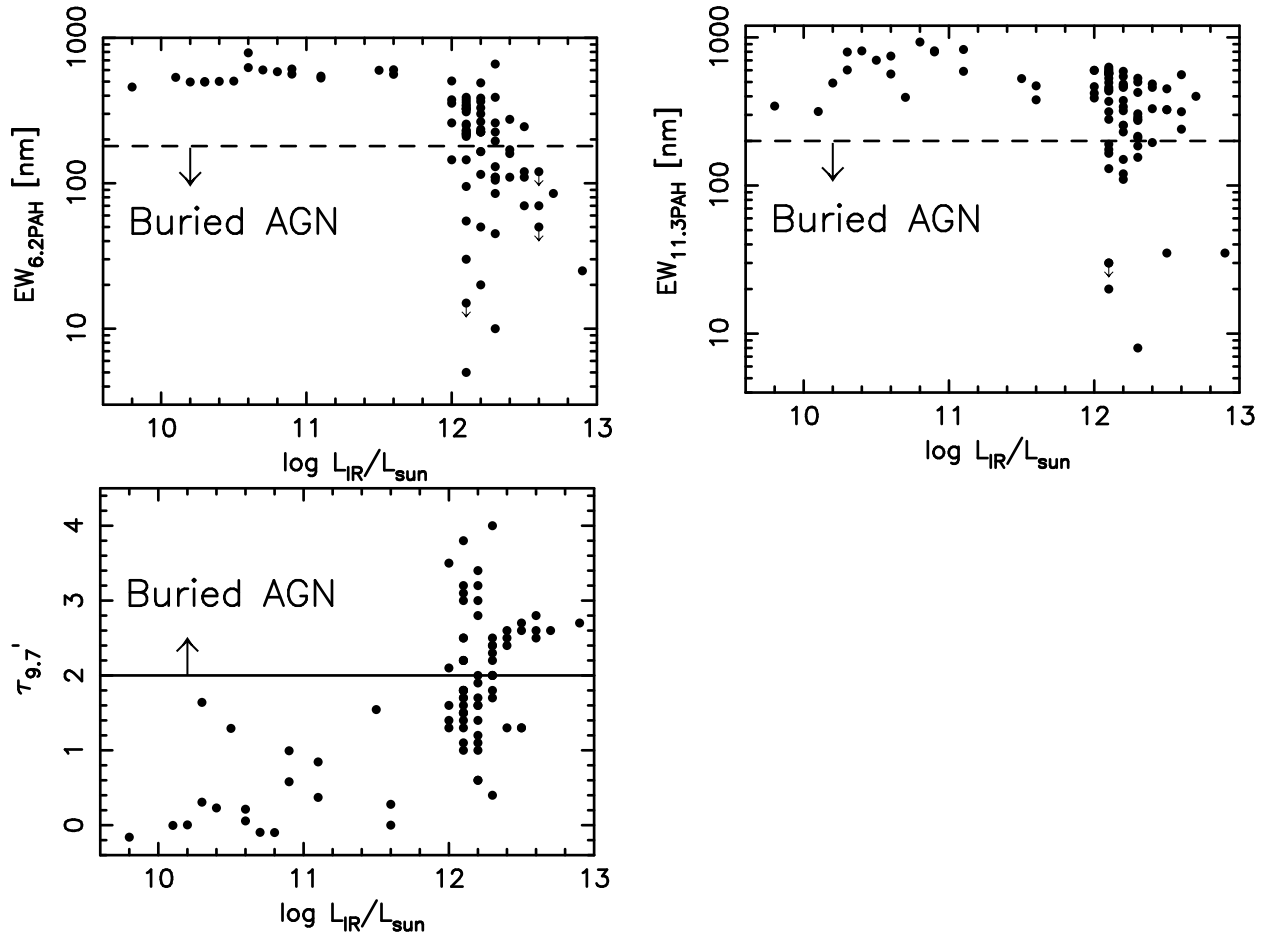


FIG. 4.— Distribution of (a) $EW_{6.2\text{PAH}}$, (b) $EW_{11.3\text{PAH}}$, and (c) $\tau'_{9.7}$, as a function of galaxy infrared luminosity. Plotted sources are optically non-Seyfert ULIRGs (This paper; Imanishi et al. 2007) and optically non-Seyfert galaxies with lower infrared luminosities (Brandl et al. 2006). The horizontal dashed lines indicate the threshold to become buried AGN candidates (§5.2.1 and 5.2.2).

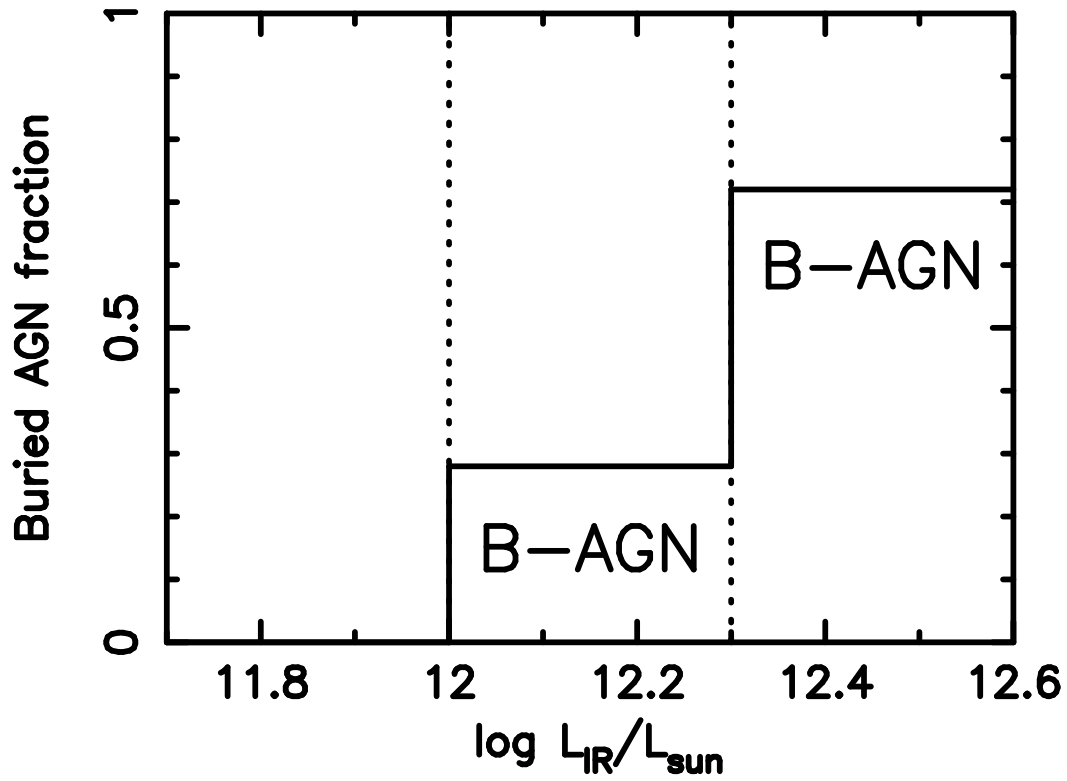


FIG. 5.— Fraction of sources with clearly detectable buried AGN signatures as a function of galaxy infrared luminosity. For ULIRGs ($L_{\text{IR}} > 10^{12}L_{\odot}$), the fraction is derived from this paper. For galaxies with $L_{\text{IR}} < 10^{12}L_{\odot}$, it is from the limited number of sample in Brandl et al. (2006), and so does not necessarily mean that no buried AGNs are present.